

# Tidal Distortion and Disruption of Earth-Crossing Asteroids

Derek C. Richardson

*Department of Astronomy, University of Washington, Box 351580, Seattle, Washington 98195-1580*  
E-mail: dcr@astro.washington.edu

William F. Bottke, Jr.

*Center for Radiophysics and Space Research, 306 Space Sciences, Cornell University, Ithaca, New York 14853-6801*

and

Stanley G. Love<sup>1</sup>

*Seismological Laboratory, California Institute of Technology, Mail Code 252-21, Pasadena, California 91125*

Received December, 19, 1997; revised April 1, 1998

We present results of numerical simulations that show that Earth's tidal forces can both distort and disrupt Earth-crossing asteroids that have weak "rubble-pile" structures. Building on previous studies, we consider more realistic asteroid shapes and trajectories, test a variety of spin rates and axis orientations, and employ a dissipation algorithm to treat more accurately collisions between the particles that make up the model asteroid. We explore a large parameter space, including the asteroid's periaipse  $q$ , encounter velocity with the Earth  $v_{\infty}$ , spin period  $P$ , initial spin axis orientation, and body orientation at periaipse.

We parameterize the simulation outcomes by the amount of mass stripped from the asteroid during a flyby. Our most severe disruptions result in fragment trains similar in character to the "string of pearls" created when Comet D/Shoemaker–Levy 9 was disrupted near Jupiter in 1992. Less catastrophic disruptions cause material to be stripped off in more isotropic fashion, leaving a central remnant with a characteristic distorted shape. Some ejecta can enter into stable orbits around the remnant, creating a binary or multiple system. Even when no mass is lost tidal forces and torques can modify the asteroid's shape and spin.

Our results show that mass loss is enhanced for small values of  $q$ ,  $v_{\infty}$ , and  $P$ , and depends to a certain extent on the body's initial spin orientation (for example, retrograde rotation reduces mass loss). An elongated asteroid was found to be far easier to disrupt than a spherical one, though the orientation of the ellipsoid at periaipse can noticeably change the outcome. The size and orbital distribution of the ejecta are discussed, along with the applications of this technique towards an under-

standing of doublet craters, crater chains, and asteroids with peculiar shapes and spins. © 1998 Academic Press

**Key Words:** asteroids, dynamics; asteroids, rotation; tides, solid body; cratering, terrestrial; computer techniques.

## 1. INTRODUCTION

### 1.1. Evidence for "Rubble-Pile" Asteroids

There is an increasing body of evidence to suggest that most kilometer-sized asteroids and comets are "rubble piles," collections of smaller fragments held together by self-gravity. If true, Earth-crossing asteroids (ECAs) should be susceptible to tidal distortion and disruption during close encounters with the terrestrial planets. Chapman (1978) was one of the first to propose seriously that high velocity collisions between asteroids in the main belt could fracture and erode monolithic bodies into "piles of boulders." This scenario was given new credibility when 243 Mathilde, a ~53-km C-type main-belt asteroid, was imaged by the Near-Earth Asteroid Rendezvous (NEAR) spacecraft in June 1997. Several surprisingly large craters—between 20 and 30 km in diameter—were seen on Mathilde's illuminated surface (Yeomans *et al.* 1997). Numerical hydrocode models of asteroid collisions suggest that craters this large could have formed only in the "gravity-scaling" regime, where the growth and ultimate size of a crater is controlled by the target's gravity rather than by physical strength (Greenberg *et al.* 1994, 1996, Asphaug *et al.* 1996, Love and Ahrens 1996). Craters formed in the gravity regime require a weak or fragmented target much like a rubble pile. Such craters cannot form in the

<sup>1</sup> Now at Jet Propulsion Laboratory, Mail Stop 306-438, 4800 Oak Grove Drive, Pasadena, CA 91109.

“strength” regime; instead such an impact would have disrupted the target if it were a monolithic body of unshattered rock. Supporting the rubble-pile idea is Mathilde’s estimated density,  $\sim 1.3 \text{ g cm}^{-3}$ , or roughly half that of carbonaceous chondrites (Wasson 1985). If C-class asteroids are indeed the parent bodies of this meteorite class (Wasson 1985), then the interior of Mathilde must either contain large void spaces or consist of small fragments with substantial interparticle porosity. Either structure is inconsistent with the conventional picture that asteroids are monoliths left intact after billions of years of impacts.

Numerical hydrocode models reveal how rubble piles may be formed. When a moderate-sized body strikes a solid target, the crater excavation is preceded by an advancing shock front that shatters the material as it passes through. Thus, even a single impact can change an initially undamaged asteroid into a highly fractured one consisting of large blocks of material. Subsequent collisions will continue to do damage, though the discontinuous inner structure of the target will make it difficult for the shock front to propagate beyond the boundaries of individual boulders near the impact site (Asphaug *et al.* 1996). Rubble piles, therefore, are even harder to disrupt or pulverize than solid objects (Love *et al.* 1993).

Images of large craters on 243 Ida, 951 Gaspra, and Phobos lend credence to this theory: Ida, with dimensions of  $60 \times 26 \times 18 \text{ km}$ , has one  $\sim 23\text{-km}$  crater and five  $\sim 10\text{-km}$  craters (Belton *et al.* 1994b, Thomas *et al.* 1996); Gaspra, with dimensions of  $18 \times 11 \times 9 \text{ km}$ , could have as many as eight craters larger than 4 km in diameter (Belton *et al.* 1994a, Greenberg *et al.* 1994); Phobos (dimensions  $27 \times 22 \times 19 \text{ km}$ ) is dominated by the large 11-km crater Stickney (Asphaug and Melosh 1993). Numerical hydrocode simulations of these crater-forming events indicate the target, in each case, is left with a highly damaged and fragmented structure (Asphaug and Melosh 1993, Greenberg *et al.* 1994, 1996).

Since most Earth-crossing asteroids are thought to be fragments of shattered main-belt asteroids which have been delivered to the terrestrial planet region by the 3:1 mean-motion and  $\nu_6$  secular resonances (Wisdom 1983, Morbidelli and Moons 1995, Gladman *et al.* 1997), we claim that most (if not all) ECAs larger than a few hundred meters in diameter are rubble piles (Love and Ahrens 1996, Melosh and Ryan 1997). Alternatively, the rubble-pile structure of small bodies may be primordial, due to preferential formation of icy or rocky components in a narrow size range (Weidenschilling 1997). In this case, collisions may not be required to achieve a rubblized state.

Either view is supported by the spin period distribution of asteroids, compiled by Harris (1996). Harris derived the critical density  $\rho_c$ , below which the centrifugal acceleration of an elongated body rotating with spin period  $P$  exceeds

its gravitational acceleration, at which point it begins to shed mass along its equator,

$$\rho_c \sim \left(\frac{3.3 \text{ h}}{P}\right)^2 \left(\frac{a}{b}\right) \text{ g cm}^{-3} \sim \left(\frac{3.3 \text{ h}}{P}\right)^2 (1 + \Delta m) \text{ g cm}^{-3}, \quad (1)$$

where the ratio of the rubble pile’s long axis to its spin axis is  $a/b$  and the lightcurve amplitude of the body has magnitude  $\Delta m$ . Plotting lightcurve amplitudes *vs* spin period for 688 asteroids of all sizes, Harris found that no asteroid spins faster than the disruption limit for a density of  $\rho_c \sim 2.7 \text{ g cm}^{-3}$ . He then examined the spin period distribution of the 107 asteroids smaller than 10 km diameter in his sample, many of which are ECAs. Harris found that this distribution abruptly truncates at fast spin rates. Since asteroids with tensile strength can rotate to high speeds, this truncation implies that ECAs may have no tensile strength and therefore may be rubble piles.

There is considerable evidence that some comets may also be rubble piles. Indirect observational and theoretical considerations (e.g., “spontaneous” nucleus splitting (Weissman 1982), formation through accretion of smaller icy components (Weidenschilling 1997), etc.) and the more direct record of tidally disrupted comets together strongly imply that comets are intrinsically weak objects.

Without question, the most famous disrupted comet is D/Shoemaker–Levy 9 (SL9), which broke into more than 20 similar-sized fragments during its penultimate encounter with Jupiter in 1992, when it passed within 1.6 jovian radii of the planet center (Sekanina *et al.* 1994). Asphaug and Benz (1996) found that SL9’s disruption into a “string of pearls” could have occurred only if the comet were virtually strengthless (cf. Section 1.2). Another tidally disrupted comet (of less renown) is P/Brooks 2, which broke into at least 8 fragments when it approached within 2 jovian radii of Jupiter in 1886 (Sekanina and Yeomans 1985). However, not all objects break apart on close approach: Comet P/Gehrels 3 remained intact after approaching within 3 jovian radii of Jupiter (Rickman 1979, Rickman and Malmort 1981), though this result is consistent with the tidal disruption limit predicted by Sridhar and Tremaine (1992) (cf. Eq. (3), below).

At least three Sun-grazing comets are believed to have been pulled apart by solar tides over the past  $\sim 100$  years: P/Great September Comet (1882), P/Pereyra (1963), and P/Ikeya–Seki (1965) (Weissman 1980). In the case of P/Ikeya–Seki, Öpik (1966) argued that the seven identifiable fragments, all of which had perihelia near 0.008 AU but diverse aphelia separated by as much as 6 AU, required a dynamic separation mechanism like tidal disruption. Typical comet-splitting mechanisms (e.g., pressure release from volatile gas pockets, explosive radicals, amorphous ice) would produce velocities of only a few meters per

second. Öpik also determined that if the comet did not have a rubble-pile structure, it would have to be weaker than “meteoric dustballs” to disrupt tidally.

The fragmentation of these comets vividly demonstrates how even weak differential gravity can drastically alter the morphology of small bodies in the Solar System. The frequency of SL9 events near Jupiter is uncertain, but the cratering records of the Galilean satellites suggest that SL9 was not a singular occurrence. Unusual crater chains called catenae, classified as having long, linear rows of equally spaced, similarly sized craters, have been identified on the Jupiter-facing hemispheres of Ganymede and Callisto (Schenk *et al.* 1996). Melosh and Schenk (1993) have suggested that the catenae are impact scars from SL9-like fragment trains, especially since their morphology and location are inconsistent with secondary chains formed by crater ejecta. Since both Ganymede and Callisto are relatively small targets far from Jupiter, SL9-type events would need to occur every 200–400 years to produce the observed number of catenae on each body (Schenk *et al.* 1996). Thus we can infer that tidal disruption is common near Jupiter.

We hypothesize that tidal disruption may also occur near Earth. Earth is smaller than Jupiter, but it is also denser, enhancing the strength of tidal forces. It is also approached more often by slow-moving asteroids than by high-speed comets; the higher density of asteroids makes them harder to pull apart, but their lower speeds allow more time for tidal forces to work. Since we have yet to observe an event comparable to SL9 in the terrestrial region, however, we must look for less direct indications.

Three main lines of evidence have emerged which support our hypothesis. First, surveys of the lunar surface have revealed one or two catenae on the Moon’s near side analogous to those seen on the Galilean satellites (Melosh and Whitaker 1994, Wichman and Wood 1995). These could have resulted from SL9-like disruption of ECAs (Bottke *et al.* 1997). Second, doublet craters—impact structures that are thought to be formed by two asteroids striking a planetary surface at nearly the same time—have been found on Earth, the Moon, Venus, and Mars (Melosh and Stansberry 1991).<sup>2</sup> These exceptional features can be explained by the impact of well-separated binary asteroids produced by tidal disruption events near terrestrial planets (Bottke and Melosh 1996a,b). Finally, delay-Doppler radar images of near-Earth asteroids (Ostro 1993) reveal bizarre shapes that may have resulted from tidal distortion during close encounters with Earth (Bottke *et al.* 1998b): asteroids 4769 Castalia, 4179 Toutatis, and 2063 Bacchus look like dumbbells, while 1620 Geographos has a highly elongated porpoise-like profile.

In this paper, we will investigate whether the tidal field

of Earth is capable of producing some (or most) of the phenomena described above. Note that even though we focus our attention on Earth, our results, to first order, should also apply to Venus, which has nearly the same size, density, and orbital position as Earth, and is encountered by roughly the same population of objects. We use a direct  $N$ -body model which simulates close encounters of rubble-pile progenitors with Earth. After characterizing various types of tidal disruption regimes, we compare our results to the observations outlined above. Our conclusions indicate that tidal disruption must now be considered an important mechanism for understanding the evolution of ECAs and other near-Earth objects.

## 1.2. Previous Work on Tidal Disruption

Boss *et al.* (1991) stated that most of the literature on tidal processes can be divided into two broad, sometimes overlapping categories: “tidal failure,” where a body with material strength undergoes tidal stresses until fracture and/or failure is induced, and “tidal disruption,” where a body is separated into two or more fragments whose orbits diverge following a planetary encounter. Here we briefly review the papers which concentrate on tidal disruption.

Roche (1847; see Chandrasekhar 1969) showed that a self-gravitating synchronously rotating liquid satellite circling a spherical planet has no stable equilibrium figure inside a critical distance,

$$r_{\text{Roche}} = 1.52 \left( \frac{M_{\text{pl}}}{\rho_{\text{sat}}} \right)^{1/3} = 2.46 R_{\text{pl}} \left( \frac{\rho_{\text{pl}}}{\rho_{\text{sat}}} \right)^{1/3}, \quad (2)$$

where  $M_{\text{pl}}$ ,  $R_{\text{pl}}$ , and  $\rho_{\text{pl}}$  are the mass, radius, and density, respectively, of the planet, and  $\rho_{\text{sat}}$  is the density of the satellite. Thus, a strengthless body with a density of  $2 \text{ g cm}^{-3}$  disrupts only if it orbits Earth at a distance less than  $3.4 R_{\oplus}$ , where  $R_{\oplus}$  is Earth’s radius.

Jeffreys (1947) and Öpik (1950) applied these ideas to calculate the tidal stress induced inside a solid satellite. Comparing those values to the strength of rock (e.g., asteroids and rocky satellites) and ice (e.g., comets and icy satellites), they concluded that tidal disruption of solid objects in the Solar System was unlikely to occur unless the satellite was unusually large and close to a planet. Both predicted that the rings of Saturn could not have been formed by the tidal disruption of a solid satellite. Including the satellite’s self-gravity into the theory, however, Öpik (1966) demonstrated that tidal forces should be important for bodies with weak internal structures (e.g., comets). Öpik even suggested that Comet Ikeya–Seki, which broke up during its close approach to the Sun in 1965, may have had a rubble-pile structure.

Sekiguchi (1970) examined whether lunar tides were strong enough to distort or disrupt asteroids before impact,

<sup>2</sup> Doublet craters may also exist on Mercury, but we are unaware of any searches that have been carried out to find them.

in the hope that they might explain many of the more unusual craters on the Moon’s surface. Though he was the first to consider this possibility, several errors have now been found in his technique, making his interpretations questionable (Dobrovolskis 1990). Aggarwal and Oberbeck (1974) later expanded on Sekiguchi’s work to investigate various modes of fracture in elastic impactors and orbiting satellites.

Dobrovolskis (1982) modeled tidal fracture in a homogeneous triaxial ellipsoid and applied his model to Phobos and other bodies. His results indicated that martian tidal forces are attempting to stretch Phobos along its long axis, but that it is stable at its present distance from Mars.

Mizuno and Boss (1985) used a numerical grid-based hydrocode with viscosity to study the tidal disruption of 1000-km planetesimals passing by an Earth-sized planet on a parabolic trajectory. Their results showed that internal dissipation can prevent tidal disruption, even when the planetesimals are on near-Earth-grazing trajectories. Kaula and Beachey (1984), using a related method, found similar results. Dobrovolskis (1990) and Sridhar and Tremaine (1992), however, questioned whether the dissipation model used by Mizuno and Boss (1985) was realistic: actual planetesimals, they argued, may not be strongly dissipative. To emphasize this point, Dobrovolskis (1990) examined how realistic failure affected tidal disruption in homogeneous objects composed of both ductile (e.g., iron) and brittle (e.g., stone or ice) materials. His results set strict limits on the size, strength, material properties, and orbital parameters required to produce a breakup event.

Melosh and Stansberry (1991), while investigating the formation of doublet craters on Earth, tested whether contact-binary asteroids (i.e., two-component rubble piles) could be pulled apart by tidal stresses just prior to impact. They found that this scenario, in general, causes only separation in a direction along the impact trajectory, such that the binary components tend to strike very close to one another. Related papers by Farinella (1992), Farinella and Chauvineau (1993), and Chauvineau *et al.* (1995) investigated the effects of planetary tides on binary asteroids. They found that close encounters modify the separation distance between the components, frequently increasing the semimajor axis and eccentricity of their mutual orbit. Accordingly, strong perturbations often cause binary components to collide or escape one another.

Boss *et al.* (1991), using a “smoothed particle hydrodynamics” (SPH) model, explored whether nonrotating, self-gravitating, inviscid planetesimals encountering the Earth suffer tidal disruption. They found that large ( $0.1 M_{\oplus}$ ) planetesimals remain intact, mostly because their size limits the approach distance to  $\sim 0.5 R_{\oplus}$ . Small ( $0.01 M_{\oplus}$ ) planetesimals were found to disrupt when their encounter velocities were less than  $2 \text{ km s}^{-1}$  and their close approach distances were less than  $1.5 R_{\oplus}$  from the center of Earth.

Boss *et al.* (1991) also discovered that Earth’s tidal forces induce elongation and spin-up in the planetesimal which often culminates in mass-shedding. Interestingly, some of their test cases revealed SL9-like outcomes nearly 2 years before the discovery of SL9 itself.

Sridhar and Tremaine (1992) developed an analytical methodology to ascertain how nonrotating, self-gravitating, viscous bodies undergo tidal disruption during parabolic encounters with a planet. They showed that such bodies shed mass if their periape is smaller than

$$r_{\text{disrupt}} = 0.69 r_{\text{Roche}} = 1.05 \left( \frac{M_{\text{pl}}}{\rho_{\text{pro}}} \right)^{1/3} = 1.69 R_{\text{pl}} \left( \frac{\rho_{\text{pl}}}{\rho_{\text{pro}}} \right)^{1/3}, \quad (3)$$

where  $\rho_{\text{pro}}$  is the body’s density (i.e., the same parameter as  $\rho_{\text{sat}}$  from Eq. (2); we use a different symbol to emphasize the progenitor’s parabolic trajectory). Their results, like those of Boss *et al.* (1991), showed that weak objects can undergo SL9-type disruptions. Since the progenitors used by Sridhar and Tremaine started in a vorticity-free state, however, and vorticity in their model could not be generated without viscosity, they were unable to investigate tidal spin-up mechanisms.

Watanabe and Miyama (1992) modeled tidal interactions between inviscid planetesimals of comparable size that encounter one another at very low relative velocities (i.e., less than the planetesimals’ mutual escape velocity). They found that fluid bodies on near-collision trajectories can be strongly deformed, almost doubling the coalescence cross-section in some cases.

Asphaug and Benz (1994, 1996), along with several other groups (e.g., Boss 1994, Sekanina *et al.* 1996, Rettig *et al.* 1996) investigated the tidal disruption of SL9 using numerical and analytical techniques. We focus on the results of Asphaug and Benz (1996), however, since their extensive test results provide a good fit to observational constraints and because their methods are closely related to our own. Asphaug and Benz (1996) tested two types of cometary progenitors: a nonrotating solid sphere, using their SPH code with material strength (Benz and Asphaug 1994), and a spherical rubble pile of equal-sized particles, using a particle tree code with “soft” elastic collisions. In the former case, they found that solid comets fracture and split under tidal stresses in binary fashion, regardless of the comet’s material properties. This hierarchical splitting (i.e., two pieces, four pieces, eight pieces, etc.) was considered too slow and difficult to create the more than 20 roughly equal-sized fragments comprising SL9. A better match was found with the rubble-pile model. With SL9’s orbital constraints, they found that Jupiter’s tidal forces could pull the pile into an elongated needle-like structure which, as it receded from Jupiter, clumped into multiple, roughly equal-sized fragments.

Bottke and Melosh (1996a,b) investigated how rotating contact-binary asteroids might disrupt during close approaches with Earth and other terrestrial planets. They found that tidal forces frequently cause these bodies to undergo fission, pulling them into separated components which can begin to orbit one another. Their results suggested that as many as 15% of the kilometer-sized Earth-crossing asteroids may have binary companions produced by this mechanism, enough to explain the large fraction of doublet craters seen on Earth ( $\sim 10\%$ ). Comparisons of the theoretical prediction with the doublet crater populations on Venus (Cook *et al.* 1998) and Mars (Melosh *et al.* 1996) also yielded good matches.

Finally, Solem and Hills (1996) investigated how Earth’s tidal forces might modify the shapes of many Earth-crossing asteroids. Using a nonrotating spherical aggregate as their progenitor, they found that close Earth approaches often kneaded the body into an elongated shape reminiscent of highly elongated asteroids such as 1620 Geographos.

In general, the studies outlined above have been concerned with nonrotating spherical fluids or particle aggregates encountering planets on parabolic trajectories. Our study treats a wider range of more realistic initial conditions. The rubble piles we examine have elongated shapes and a variety of spin rates and spin axis orientations at encounter. We also give them hyperbolic planetocentric trajectories, allowing us to test a variety of encounter velocities and periaipse distances. By systematically sampling each of these parameters we can estimate the rate of tidal distortion and disruption near Earth of real ECAs. As we will show, tidal forces play an important role in the evolution of the ECA population, one that may have been underestimated in the past.

## 2. METHOD

### 2.1. Tidal Disruption Model

The rubble piles in our simulations are qualitatively similar to those used previously by Asphaug and Benz (1996) and others: they are roughly the same size, they have approximately the same number of particles, and they are held together only by self-gravity. Specifically, the progenitor is an aggregate of 247 identical spherical particles, each 255 m in diameter. The number of particles was chosen as a compromise between resolution and computation time: each individual run takes several hours to complete on a 200-MHz Pentium running Linux.

The previous studies of rubble piles found some general, largely intuitive trends: tidal breakup is most severe when the rubble pile passes close to the planet and when tidal forces have a longer time to act. We might reasonably expect spin and nonsphericity to enhance this process by reducing the effective gravity at points on the surface that

are furthest from the rubble pile’s center. In order to explore these issues, we have made our simulations more realistic by introducing several enhancements over previous studies:

1. **Nonsphericity:** We investigated two different configurations for our rubble piles: a nearly spherical close-packed progenitor (cf. Asphaug and Benz 1996) and an ellipsoidal one that more closely resembles real Earth-crossing objects (McFadden *et al.* 1989, Ostro 1993, Ostro *et al.* 1995a,b). In the latter case, the body had initial dimensions of  $2.8 \times 1.7 \times 1.5$  km ( $1.8 \times 1.1 \times 1.0$  normalized), not unlike the axis ratio of 4769 Castalia (Hudson and Ostro 1994). We chose the elongated shape because spherical progenitors (used by all other groups) have lower gravitational potential energies and suffer smaller maximum tidal stress, making them intrinsically more stable against tidal disruption than more general configurations. The elongated shape was obtained by distorting a spherical progenitor. We have tested the stability of the elongated progenitor over time scales an order of magnitude longer than the duration of the runs performed here. No significant shape changes were seen.

2. **Rotation:** We let the progenitors rotate over a range of spin periods and spin axis orientations. The spherical progenitor was tested for a spin period of  $P = 6$  h, while elongated progenitors were tested for  $P = 4, 6, 8, 10, 12$  h, and  $P = \infty$  (i.e., no spin). Most earlier models used progenitors without spin since (a) it is simpler and (b) objects with random spin axis orientations have a nearly equal probability of encountering a planet with a prograde or retrograde spin, making the “zero-spin” case a reasonable representative case. This “average” progenitor ( $P = \infty$ ), however, does not produce the median breakup outcome. Our results indicate that the median breakup outcome is instead dominated by objects with prograde spins, which are susceptible to tidal disruption; E. Asphaug and W. Benz (1997, personal communication) have found this same result.

3. **Hyperbolic flybys:** Hyperbolic encounters can be defined by the rubble pile’s encounter velocity at “infinity” ( $v_\infty$ , the velocity of a body before the gravitational acceleration of Earth becomes significant) and its periaipse distance ( $q$ ). The previously simulated parabolic encounters ( $v_\infty \equiv 0$ ) provide a useful approximation, but have unrealistically long flyby times.

4. **Energy dissipation:** Collisional energy loss between particles is incorporated through a coefficient of restitution  $\epsilon$  (i.e., the ratio of the rebound speed to the impact speed). For the cases in this paper,  $\epsilon = 0.8$ . Our tests show that tidal disruption is largely insensitive to the choice of  $\epsilon$  so long as collisions are inelastic ( $\epsilon < 1$ ) (also seen by E. Asphaug 1997, pers. commun.). Previous models featured only elastic collisions.

The bulk density of our rubble piles was  $2 \text{ g cm}^{-3}$ . Individual particles had densities of  $3.6 \text{ g cm}^{-3}$ , similar to ordinary chondritic meteorites (Wasson 1985). Our choice of bulk density may be conservative, in light of the estimate of 253 Mathilde’s density ( $1.3 \text{ g cm}^{-3}$ ), but it is reasonable given the range of densities measured for Phobos and Deimos ( $\sim 2 \text{ g cm}^{-3}$ ; Thomas *et al.* 1992) and 243 Ida (between  $2.1$  and  $3.1 \text{ g cm}^{-3}$ ; Belton *et al.* 1995). We have decided to omit test runs with low cometary bulk densities ( $\sim 1 \text{ g cm}^{-3}$ ) because we do not expect many comets to disrupt tidally near Earth. Long-period comets typically have such high encounter velocities with Earth (the mean encounter speed is  $\sim 55 \text{ km s}^{-1}$ ; Weissman 1982) that few are expected to undergo tidal disruption, despite their lower bulk density. The contribution of short-period comets to the near-Earth object population is thought to be negligible (Morrison 1992). We chose not to address the issue of extinct comets within the Earth-crossing asteroid population at this time.

## 2.2. Complications Using Rotating, Elongated Rubble Piles

Allowing rubble piles to rotate significantly increases the complexity of the simulation and the size of parameter space that must be investigated to adequately characterize tidal disruption outcomes. For example, an object that disrupts during a close approach when rotating prograde (i.e., in the same sense as the orbit) may not disrupt if the spin is retrograde. Our results will show that the quantity of mass shed during a disruption event depends on the orientation of the body’s spin axis at periape with Earth (perigee). We define this orientation by two angles:  $\alpha$ , the angle between the rotation pole and the  $z$  axis, measured relative to a Cartesian coordinate system (Fig. 1), and  $\beta$ , the angle between the rotation pole projected onto the  $xy$  plane and the  $-x$  axis. Thus, prograde spins have  $\alpha < 90^\circ$ , while retrograde spins have  $\alpha > 90^\circ$ .

Use of a nonspherical progenitor also complicates matters. We find that the orientation of the body’s long axis at perigee affects the amount of mass shed during tidal disruption. Consequently, we keep track of the rubble pile’s rotation phase, using the angle  $\theta$  (Fig. 1). When  $\theta = 0^\circ$ , the long axis (or its projection in the orbit plane) points directly toward Earth. When  $\alpha < 90^\circ$  (prograde rotation) and  $0^\circ \leq \theta \leq 90^\circ$ , the leading long axis of the object is rotating toward Earth just before close approach. Conversely, when  $\alpha < 90^\circ$  (prograde) and  $90^\circ \leq \theta \leq 180^\circ$ , the leading long axis is rotating away from Earth.

## 2.3. Description of Numerical Technique

The numerical code and methods described here follow Richardson (1993, 1994, 1995). All computations are three-dimensional, with no limit to the spatial domain that can

be occupied by the particles. We directly integrate the equations of motion including the particles’ self-gravity. Although this method scales as  $N^2$ , where  $N$  is the number of particles in the rubble pile, we use relatively few particles ( $\leq 1000$ ) so that there is little advantage to employing cost-reducing algorithms such as hierarchical trees. A typical run with a 247-particle aggregate involves over half a million collisions in about 5 million time steps.

Our numerical integrator is a fourth-order predictor–evaluator–corrector scheme that features individual particle time steps (Aarseth 1985). The individual steps are critical in order to detect collisions accurately (Richardson 1994). Optimal steps are calculated with an empirical formula, parameterized by a dimensionless coefficient, that uses the force and its higher order time derivatives (Press and Spergel 1988). It should be emphasized that collisions between particles are detected *ex post facto*. That is, collisions are detected at any given step by noting whether there is physical overlap between the current particle and its nearest neighbor. For the bulk of the runs discussed here, the coefficient in the time step formula was chosen such that overlaps are typically no greater than 0.1% of the sum of the radii of the colliding pair. This parameter choice has been found to limit nonphysical numerical drift in angular momentum adequately ( $< 5\%$  maximum deviation) over the course of a typical rubble-pile asteroid encounter with Earth. Encounters completed with smaller time step coefficients (i.e., greater accuracy at the cost of computational efficiency) show no significant differences. For our simulations, all particles are modeled as indestructible uniform spheres. The particles lack sticking forces, such that agglomeration arises solely from self-gravity.

As mentioned previously, each model incorporates a normal coefficient of restitution  $\epsilon = 0.8$ . There is no surface friction in the models (i.e., the transverse restitution coefficient is unity). Without energy dissipation, any clumps that form by gravitational instability are noticeably less tightly bound. For collisions at small relative speeds, however ( $v \lesssim \frac{1}{3}v_{\text{esc}}$ , where  $v_{\text{esc}} \sim 18 \text{ cm s}^{-1}$  is the surface escape speed of a particle in our simulations), it is necessary to adopt  $\epsilon = 1.0$  to prevent computationally expensive surface sliding motions (Petit and Hénon 1987). A minimum time-step  $\delta t_{\text{min}}$  of  $10^{-10}$  time units (one time unit =  $1/2\pi$  year) is imposed to ensure that time stepping does not venture too close to the limits of machine precision. Also, a maximum step of 0.01 time units is used to ensure a minimum integration accuracy for particles that have drifted far from their perturbing neighbors. Richardson (1994) gives additional details regarding the precise calculations needed to handle collisions in a dense self-gravitating environment such as a rubble pile.

It is interesting to note that the rubble piles in our simulations behave somewhat like fluids, particularly at the moment of disruption. That is, the rubble pile is seen to flow

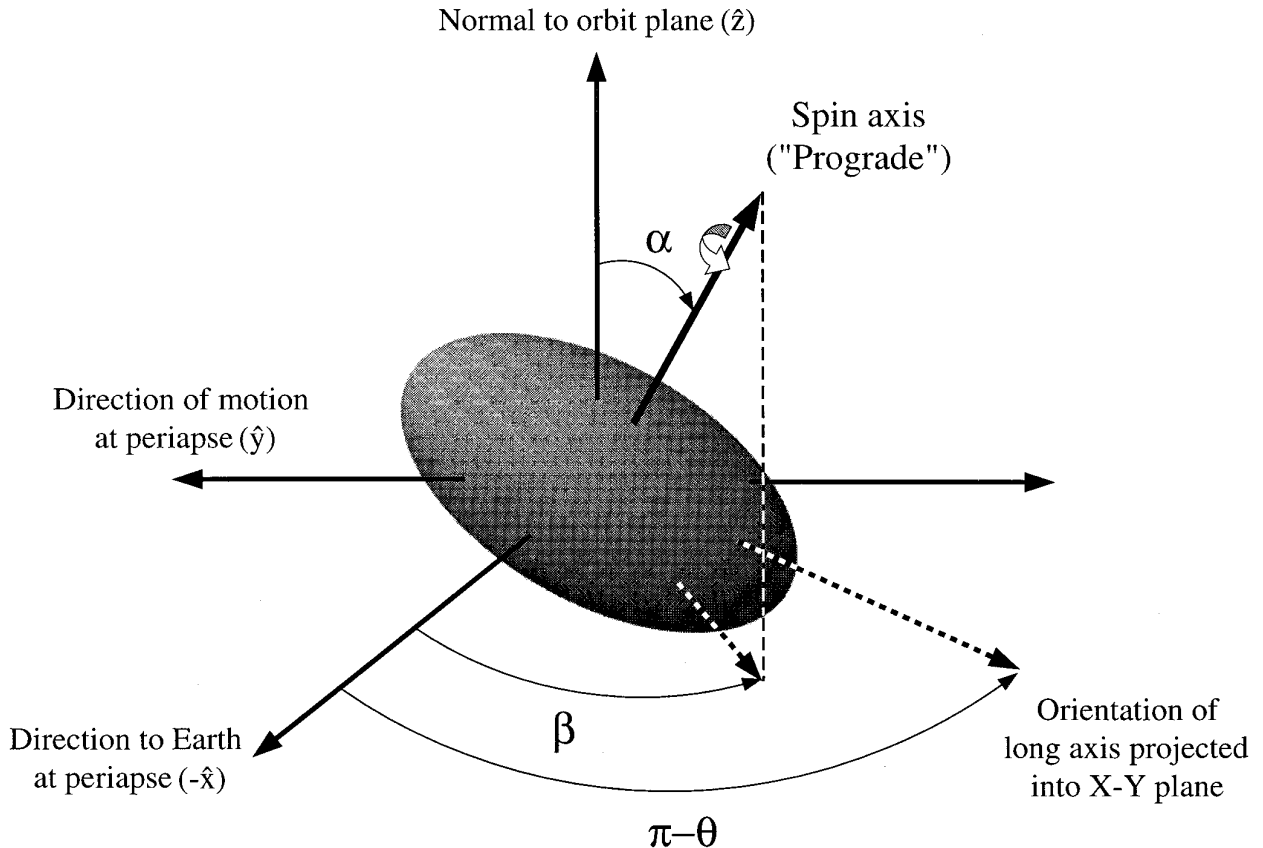


FIG. 1. Diagram illustrating the two spin axis orientation angles  $\alpha$  and  $\beta$  and the body orientation angle  $\theta$  measured in the orbit plane. The quantity  $\pi - \theta$  is shown, rather than  $\theta$  directly, to avoid crowding the figure. The nonrotating Cartesian coordinate system is defined with the  $x$  axis pointing away from the planet at periaapse, the  $y$  axis pointing in the direction of motion at periaapse, and the  $z$  axis pointing normal to the orbit plane as illustrated.

smoothly from one form to another during disruption. Indeed, it has been found that under some circumstances (usually after free-fall accretion), a rotating rubble pile has a shape consistent with a Jacobi ellipsoid (cf. Binney and Tremaine 1987; also see Section 4.1.5). However, not all rubble piles are Jacobi ellipsoids, owing to the finite size of the constituent particles: the rubble pile can get trapped in a local energy minimum that requires a finite input of energy before the material can reconfigure itself into a lower energy state. This effect is similar to the angle of repose of granular media, a concept that depends only on the material properties of the grains (e.g., Pöschel and Buchholtz 1993). Because of this, our progenitors generally maintain their shapes prior to Earth encounter despite different initial rotation rates. Finite-size effects also make the rubble piles slightly more difficult to disrupt than the truly fluid objects studied by Sridhar and Tremaine (1992), though we believe that they also cause the bodies to behave more like real comets and asteroids.

To minimize round-off error when particle separations are computed, we carry out the simulations in the rubble

pile's center-of-mass frame. The equation of motion for the  $i$ th particle is then written

$$\ddot{\mathbf{r}}_i = \mathcal{F}i - \frac{GM_\oplus}{R_\oplus^3} \mathbf{R}_\oplus, \quad (4)$$

where

$$\mathcal{F}i = - \sum_{j \neq i} \frac{Gm_j}{|\mathbf{r}_i - \mathbf{r}_j|^3} (\mathbf{r}_i - \mathbf{r}_j) \quad (5)$$

is the force per unit mass on the  $i$ th particle due to the other rubble pile particles and Earth. The second term in Eq. (4) represents the acceleration of the center-of-mass frame by Earth and is calculated to high order in the position vector. Note that in this model, the force contribution of Earth is treated like that from any other point-mass (i.e., in the summation,  $m_0 \equiv M_\oplus$ ,  $\mathbf{r}_0 \equiv \mathbf{R}_\oplus$ , and shape effects are ignored), although the back-reaction of the rubble pile particles on Earth is neglected. Also, neither the

tidal effect of the Sun nor the perturbing effect of the Moon have been included in these calculations. As we are primarily interested in the mechanics of tidal breakups, such small perturbing effects can be ignored.

The asteroid is taken to start 15 Roche radii from Earth (recall  $R_{\text{Roche}} \sim 3.4 R_{\oplus}$  for a body with bulk density  $\rho_{\text{bulk}} = 2 \text{ g cm}^{-3}$  in the vicinity of Earth), large enough to ensure that Earth’s perturbations are negligible at the outset, but small enough to make exploration of parameter space practical. Each run is terminated at a post-encounter distance of  $\sim 60 R_{\oplus}$ , the distance between Earth and the Moon. See Appendix A for a derivation of the total integration time for these orbits, parameterized by  $q$  and  $v_{\infty}$ .

During the run, the following outputs are generated periodically: summary statistics for diagnostic purposes, particle positions and velocities for analysis such as clump identification, and animation frames. Also recorded is the instant of closest approach (periapse passage) for later determination of the asteroid’s orientation at the point of maximum tidal stress.

## 2.4. Analysis Method

**2.4.1. Clump-finding algorithm.** For our interests, the most basic information that can be gleaned from a tidal encounter is the nature and amount of any shed material. Our analysis code automates the categorization of each tidal encounter by identifying the post-encounter distribution of particles. The largest (most massive) clump is taken to be the progenitor’s undisrupted remains. The outcome classes, which we define in Section 3.1, are simply determined by the mass fraction of these remains.

To find clumps, we define a “radius of influence,”

$$\mathcal{R} = \max(0.05 R_{\text{Hill}}, n_c^{-1/3} \ell_{\text{max}}), \quad (6)$$

where

$$R_{\text{Hill}} = r \left( \frac{m_c}{3M_{\oplus}} \right)^{1/3} \quad (7)$$

is the Hill radius (the characteristic distance of influence in the restricted three-body problem; here  $m_c$  is the clump mass and  $r$  is the distance of the progenitor’s center of mass from Earth),  $\ell_{\text{max}}$  is the maximum dimension of the clump, and  $n_c$  is the number of particles in the clump. Equation (6) was arrived at through trial and error and by comparing the computed clumps with a visual examination of the data. Although largely empirical in origin, this formula, when used in the clump-finding algorithm, accurately detects clumps. The use of the  $\max(\ )$  function strikes an excellent balance between gravitational association (via the Hill radius) and physical proximity.

Initially Eq. (6) is used to find the radii of influence of

individual particles (i.e., in the formula,  $n_c = 1$ ,  $m_c$  is the particle mass, and  $\ell_{\text{max}}$  is the particle diameter). Each particle is checked in turn to see whether any spheres of influence overlap. If an overlap is detected, the particles are merged together to form an “association” or “proto-clump.” The algorithm then proceeds iteratively, first recalculating radii of influence for any new associations created and then checking overlaps for both particles and associations, until after a complete pass the association membership does not change. Once this procedure terminates, any associations with 3 or more particles are considered to be clumps.

Comparisons between the algorithm’s results and a visual examination of outcomes have yielded favorable matches in nearly all cases. In addition, this simple clump-finding routine was compared with the output from SKID (J. Stadel, *et al.*, in preparation),<sup>3</sup> a generalized code developed for cosmological simulations that finds gravitationally bound groups in  $N$ -body simulations by following density gradients to a density maximum. There was no significant difference in detection accuracy found between the two methods.

**2.4.2. Properties of the post-encounter remnant.** Once clumps have been identified, the most massive clump is taken to be the remnant of the original rubble pile. The following properties are then measured:

1. Mass: To determine the relative mass of the remnant, we take the ratio of the number of particles in the clump to the total number of particles  $N$  in the simulation. Since all particles are identical, this yields the remnant’s mass fraction  $M_{\text{rem}}$ .

2. Rotation period: To determine the rotation period,  $P_{\text{rem}}$ , we first compute the inertia tensor  $\mathbf{I}$  of the clump, given by

$$\mathbf{I} = \sum_i [\mathbf{I}_i + m_i(r_i^2 \mathbf{1} - \mathbf{r}_i \mathbf{r}_i)], \quad (8)$$

where  $\mathbf{I}_i = \frac{2}{5} m_i R_i^2 \mathbf{1}$  is the inertia tensor of each constituent particle  $i$  ( $m_i$  is the particle mass and  $R_i$  the radius;  $\mathbf{1}$  is the unit matrix), and  $\mathbf{r}_i$  is the particle’s position relative to the clump’s center of mass. Next, the angular momentum of the remnant with respect to its mass center is computed according to

$$\mathbf{h} = \sum_i m_i \mathbf{r}_i \times \mathbf{v}_i, \quad (9)$$

where  $\mathbf{v}_i$  is the particle’s velocity relative to the clump’s center of mass. Note that intrinsic particle spin is ignored

<sup>3</sup> The code is publicly available from [www-hpcc.astro.washington.edu/tools/SKID/](http://www-hpcc.astro.washington.edu/tools/SKID/).

since there is no surface friction in any of the models. Now since, for a solid body,  $\mathbf{h} \equiv \mathbf{I}\boldsymbol{\omega}$ , where  $\boldsymbol{\omega}$  is the angular velocity, the remnant's rotation period is given by

$$P_{\text{rem}} = \frac{2\pi}{|\boldsymbol{\omega}|} = \frac{2\pi}{|\mathbf{I}^{-1}\mathbf{h}|}. \quad (10)$$

Note that this formalism assumes that the remnant can be treated as a rotating solid body (i.e., one in which the position vectors  $\mathbf{r}_i$  remain fixed in the body frame). In the presence of shear (such as during the actual disruption event when particles closer to the planet acquire a larger Keplerian speed than those further away), some outer particles may rotate more slowly about the mass center than the solid body rate of the core, giving rise to a somewhat longer effective period. This factor, however, does not affect our results in any significant way since spins are generally measured well after disruption.

As a result of angular momentum transferred in some tidal encounters, the final rotation generally will not be aligned with the principal axes of inertia, resulting in a complex spin state. We have made no attempt to characterize this behavior in the current study, beyond noting visually the presence of tumbling motion in some rubble piles. We can, however, estimate the characteristic time for rotational energy dissipation to return the body to principal-axis rotation,

$$\tau = \frac{\mu Q}{\rho K_3^2 R^2 \omega^3}, \quad (11)$$

where  $\mu$  is the asteroid's rigidity,  $Q$  is the quality factor,  $\rho$  is the bulk density,  $R$  is the mean radius,  $\omega$  is the angular frequency of rotation, and  $K_3^2$  is a shape factor ranging between 0.01 for nearly spherical bodies and 0.1  $H^2$  for nonspherical bodies with oblateness  $H$  (Burns and Safrosov 1973). Thus, by assuming that  $\mu Q \sim 10^{11} \text{ N m}^{-2}$ , the value determined for Phobos by Yoder (1982),  $R \sim 1 \text{ km}$ , and  $P = 6 \text{ h}$ , we estimate that any ‘‘wobble’’ induced in our progenitors by tides should last  $\sim 6 \text{ Myr}$  for elongated bodies and  $\sim 60 \text{ Myr}$  for nearly spherical bodies. Slower rotators will have much longer damping time scales, in some cases exceeding the age of the Solar System. Harris (1994) used Eq. (11) to show that some main-belt asteroids (e.g., 253 Mathilde) and near-Earth asteroids (e.g., 4179 Toutatis) with days- to weeks-long rotation periods should be found in tumbling rotation states today. Although it is unlikely that close encounters produced the slow rotation of Toutatis ( $P = 130 \text{ h}$ ; Hudson and Ostro 1995), it is possible that a planetary encounter may have provided an impulse which is still observable today (G. Black, pers. commun.). For simplicity, however, we currently treat bodies only in principal-axis rotation. The role of complex spin in tidal encounters will be the subject of future work.

3. Size: The inertia tensor is also used to calculate the clump dimensions (including the quantity  $\ell_{\text{max}}$  used in the iterative procedure described above). Note that these dimensions are not intended to describe the rotation of the body, just its linear size; the inertia tensor is used only to identify the long and short axis directions along which it seems most natural to measure those dimensions. The principal axes of the clump are obtained by diagonalizing the inertia tensor and solving for the eigenvectors (e.g., Press *et al.* 1992, Sections 11.1–11.3). This provides the body axis orientations. To compute the lengths, all possible two-body particle separations are calculated and projected onto each body axis. The largest separations  $a_1$ ,  $a_2$ , and  $a_3$  along each axis are recorded and sorted so that  $a_1 \geq a_2 \geq a_3$ . These are taken to be the clump dimensions (so  $\ell_{\text{max}} \equiv a_1$ ). Note that distances between spheres along a given axis include the finite size of the spheres (i.e.,  $2R_i$  is added to each length). In the literature, the axis ratios  $q_2 \equiv a_2/a_1$  and  $q_3 \equiv a_3/a_1$  are often used to characterize nonaxisymmetric bodies such as these clumps. In addition, we define a convenient single-value measure of the remnant's ‘‘ellipticity’’ using the quantity  $\varepsilon_{\text{rem}} \equiv 1 - \frac{1}{2}(q_2 + q_3)$ .

*2.4.3. Phase angle of the progenitor long axis at periape.* The phase angle of the progenitor long axis at periape is represented by  $\theta$  in Fig. 1 (cf. Section 2.2). The techniques described in the previous subsection can be applied to the progenitor itself just prior to disruption so that the rotation phase angle at periape can be computed,

$$\theta = \begin{cases} \cos^{-1}(\hat{\mathbf{p}}_{1,\perp} \cdot \hat{\mathbf{x}}) & \text{if } (\hat{\mathbf{p}}_1 \cdot \hat{\mathbf{y}}) \leq 0 \\ \pi - \cos^{-1}(\hat{\mathbf{p}}_{1,\perp} \cdot \hat{\mathbf{x}}) & \text{otherwise} \end{cases}, \quad (12)$$

where  $\mathbf{p}_{1,\perp} \equiv \mathbf{p}_1 - (\mathbf{p}_1 \cdot \hat{\mathbf{z}})\hat{\mathbf{z}}$  is the projection of the rubble pile's major axis  $\mathbf{p}_1$  (the eigenvector of the inertia tensor associated with  $\ell_{\text{max}}$ ) onto the  $xy$  plane, and  $\hat{\mathbf{y}}$  denotes a unit vector. The conditional eliminates the ambiguity of  $\pi$  in the orientation of  $\hat{\mathbf{p}}_1$  so that  $\theta$  is always measured clockwise from the  $-x$  axis.

*2.4.4. Osculating elements.* Finally, to categorize the material liberated from the progenitor, we determine the mass fraction of clumps that are in the process of escaping, orbiting, or reaccreting onto the remnant rubble pile. These ratios are derived by computing the osculating elements of all the other clumps with respect to the remnant. A reaccreting clump is one for which the orbital eccentricity with respect to the remnant rubble pile  $e < 1$  and for which the semimajor axis  $a \leq \ell_{\text{max}} + a_l$ , where  $a_l$  is the length of the longest body axis of the clump in question. Otherwise, if  $e < 1$ , the clump is considered to be orbiting the remnant rubble pile. If  $e \geq 1$ , the clump is escaping. The total number of particles in each category is divided by  $N$  to form the ratios.

The equations for  $a$  and  $e$  are similar to those found in Appendix A. For completeness, the orbital inclination is given by  $i = \cos^{-1}(\hat{\mathbf{h}} \cdot \hat{\mathbf{h}}_0)$ , where  $\mathbf{h}$  and  $\mathbf{h}_0$  are the relative angular momenta of the clump with respect to the remnant and the remnant with respect to the planet.

### 3. RESULTS

#### 3.1. Tidal Encounter Outcome Classes

We divide tidal encounter outcomes into four classes according to the mass  $M_{\text{rem}}$  of the largest surviving fragment:

1. Catastrophic or ‘‘SL9-type’’ disruption (S-class): The disruption is S-class when the largest remaining fragment retains less than 50% of the progenitor’s original mass (Fig. 2, leftmost column). This is the most visually dramatic of the outcome classes. At close approach, the rubble pile’s equipotential surface (that is, the surface to which a fluid would conform under the influence of local gravity and tidal and centrifugal forces) is stretched into a cigar shape lined up roughly in the direction of the planet. Like a fluid, particles adjust to conform with the new equipotential surface by moving ‘‘downhill’’ to fill in the new valleys. The strength of the landslide is limited by friction and finite-size effects. As the rubble pile recedes from the planet, it continues to stretch apart until the orbital separation time scale exceeds the free-fall time scale of the debris (Hahn and Rettig 1998). Around this time the particles start to clump into a number of roughly equal-sized bodies. This disruption type is analogous to that seen when SL9 was disrupted near Jupiter (cf. Section 1.1).

We find that the debris train length  $L$  grows almost linearly with time following S-class disruptions (Fig. 3), as expected for hyperbolic encounters (Hahn and Rettig 1998), in contrast to the  $t^{4/3}$  asymptotic growth seen in parabolic models (e.g., Sridhar and Tremaine 1992). The exact number of clumps formed depends on various parameters; Hahn and Rettig (1998) use an analytic argument to show  $n \sim L/D$ , where  $L$  is the train length at the onset of collapse (which depends on the encounter parameters and the progenitor bulk density) and  $D$  is the progenitor diameter. However, they have tested only cases of nonspinning spherical progenitors; more work is needed to generalize the theory for comparison with the cases presented here.

2. Rotational breakup (B-class): A B-class disruption occurs when the largest remaining fragment retains between 50 and 90% of its mass (Fig. 2, middle column). With this less extreme form of disruption, the tidal field again stretches the equipotential surface of the rubble pile, though not as much as before. As particles move ‘‘downhill’’ toward the ends, some may find that their centrifugal acceleration is too small to maintain rigid body rotation.

Those particles are then ejected and swept backward in the equatorial plane by the asteroid’s rotation. Material retained near the tips may preserve a spiral signature in the form of cusps pointed against the rotation direction, similar to those produced in models of stellar collisions (Benz and Hills 1987, Benz *et al.* 1989). In addition, torques on the rubble pile modify its net rotational angular momentum, making it spin up or spin down. The final rotation rate of the remnant rubble pile depends on several factors which will be discussed later in the paper.

3. Mild disruption (M-class): M-class disruptions are those for which the stripped material accounts for less than 10% of the progenitor’s mass (Fig. 2, rightmost column). In this case, only small clumps or individual particles at the limit of the model resolution are lost. In the process, however, the progenitor shape is often strongly distorted. Typically, one end suffers more elongation and mass shedding than the other, becoming long and tapered, while the other end often becomes stubbier in appearance. Some M-class outcomes resemble the final shape of at least one near-Earth asteroid imaged by delay-Doppler radar techniques (Bottke *et al.* 1998b; cf. Section 4.1.5).

4. No mass loss (N-class): For this outcome class, no mass is lost during the encounter but tidal torques may still reshape the asteroid and/or change its spin rate.

#### 3.2. Dependence on Model Parameters

There are many physical parameters that determine the tidal encounter outcome: the trajectory (two parameters; more if effects due to planetary shape are included), the rotation rate (one parameter), the spin axis orientation (two parameters), the body shape and overall size (at least three parameters), the long axis orientation at periape (one parameter), the planet/body density ratio (one parameter), the nature of the constituent rubble pile particles (many parameters), etc. We have systematically investigated the effect of changing the rubble pile’s trajectory and rotation, performed many body and spin axis orientation experiments, and studied a few shape and density models. For reasons of computational expediency, other important factors, such as the rubble pile’s size, its internal structure, and the shapes and sizes of individual particles, were not investigated at this time.

- 3.2.1. *Trajectory: Varying  $q$  and  $v_\infty$ .* For these tests we used our ‘‘generic’’ elongated asteroid with perfectly prograde rotation ( $\alpha = 0^\circ$ ; no spin-axis tilt). The spin period was set to 6 h, the median rotation period of Earth-crossing asteroids (Harris 1996). The phase angle  $\theta$  was constrained to lie between  $0^\circ$  and  $90^\circ$  in order to encourage tidal disruption (cf. Section 2.2 and discussion on  $\theta$  below).

Since tidal forces vary as the inverse cube of the distance, we expect that the perigee distance  $q$  is one of the most important parameters in tidal breakup. Our results confirm

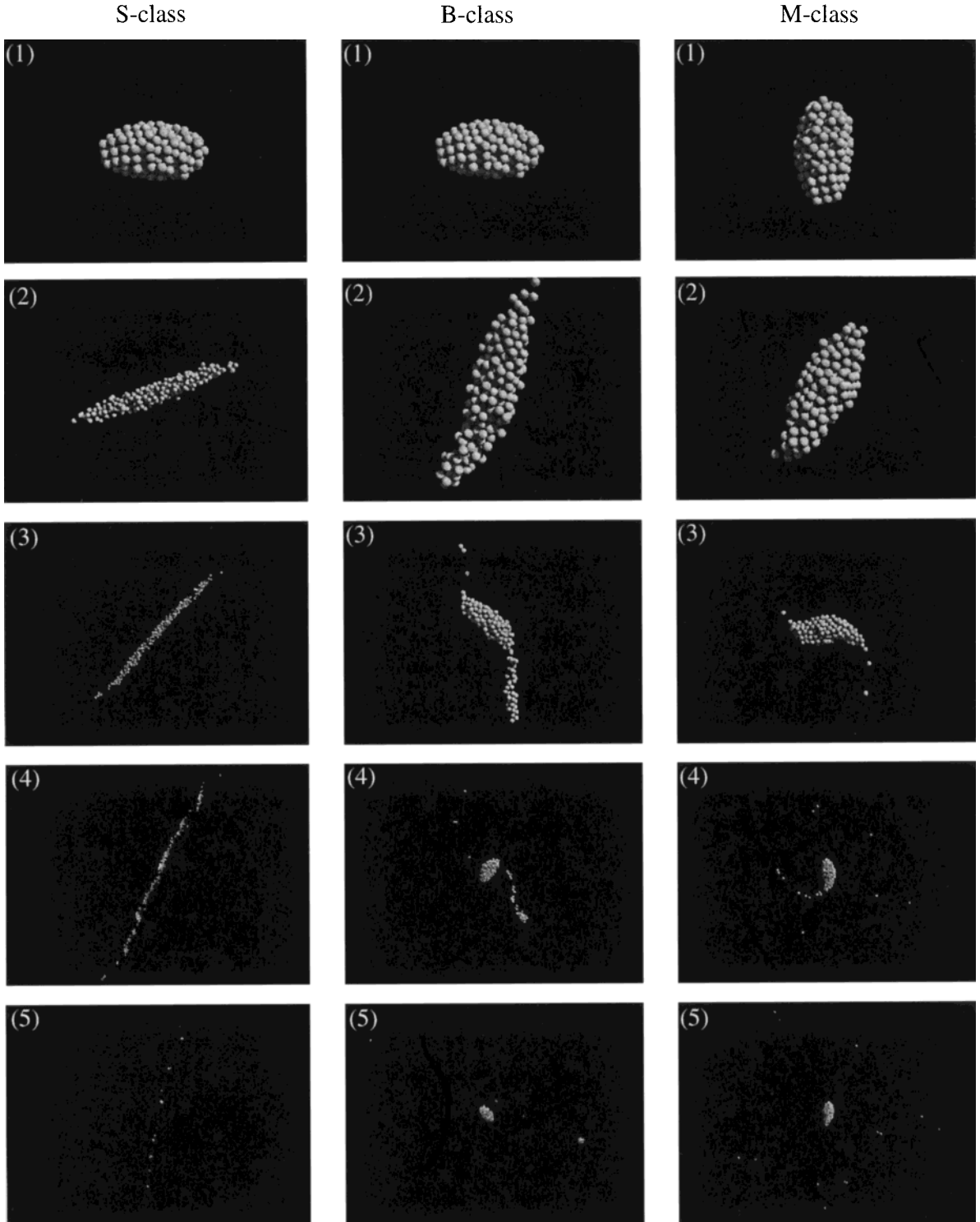


**FIG. 2.** Snapshots illustrating the evolution of the three outcome classes that involve mass loss. Time proceeds from top to bottom in each column. Frame (1) shows the start of each run and frame (5) the end. Frames (2)–(4) were selected to illustrate distinctive points in the evolution of each class, and so are not spaced evenly in time. S-class “Shoemaker–Levy-9-type” disruptions (leftmost column) typically result in the formation of a line of roughly equal-size clumps (a “string of pearls”), leaving less than 50% of the original mass in the largest fragment. More moderate B-class breakups (middle column) show mass shedding of clumps and single particles, leaving the progenitor with 50–90% of its original mass. M-class disruptions (rightmost column) exhibit milder isotropic mass shedding of clumps or particles in the orbit plane, leaving the progenitor with over 90% of its original mass. Nondisruptive N-class outcomes are not illustrated, but can result in reshaping of the progenitor accompanied by spin-up or spin-down.

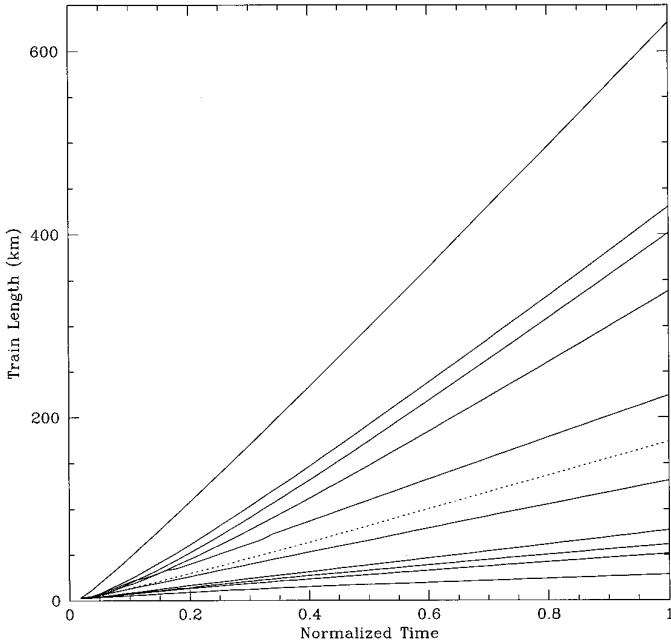


**FIG. 3.** Train lengths as a function of normalized time for the 11 S-class outcomes of the  $P = 6$  h case from Fig. 4. Time  $t = 1$  corresponds to the end of each simulation while  $t = 0$  is close to the time of perigee passage. The train length at  $t = 0$  is equal to the original progenitor size, about 2 km. Note that due to differences in the encounter speed  $v_\infty$ , the termination distances for these runs were reached at different times, which is why the abscissa has been normalized for easy comparison. Generally the faster the encounter speed, the shorter the debris train at the end of the run, simply because it has had less time to grow. The S-class case shown in Fig. 2 is indicated with a dashed line here. Note that in all cases the train lengths grow almost linearly, consistent with a hyperbolic flyby.

this strong dependence (Fig. 4): as  $q$  increases from 1.01 to  $3.8 R_\oplus$ , tidal disruption becomes less efficient, changing the outcome from S-class for the smallest  $q$  values, through B- and M-class for intermediate values, and finally to N-class for the largest  $q$  values. To illustrate this further, Fig. 5 shows the configuration of the  $P = 6$  h rubble piles at the termination of their runs. Both figures indicate that even at the slowest encounter speeds, there is a distance beyond which mass stripping no longer takes place.

The encounter velocity ( $v_\infty$ ) is also critically important. As the encounter speed  $v_\infty$  increases from 3 to  $24 \text{ km s}^{-1}$ , tidal disruption again becomes less violent. Faster encounter speeds mean less time spent near Earth where tidal forces are strongest. If  $v_\infty$  is sufficiently high, no  $q$  value will allow S-class disruption. Our results indicate that this limit is well below the mean encounter speeds of long-period comets with Earth ( $\sim 55 \text{ km s}^{-1}$ ; Weissman 1982). Thus, we predict that few comets ever undergo strong tidal disruption in the terrestrial planet region.

In general, we find that small values of  $q$  and  $v_\infty$  are needed for strong disruption to take place. Again this is

related to the penetration distance inside the Roche sphere and the time spent within the sphere: the closer the penetration point to the planet, the larger the range of encounter velocities that can lead to disruption.

As an aside, we caution that these results suffer to a limited extent from unavoidable discreteness effects, arising both from the practical limitations of exploring parameter space with high resolution and the complications introduced by variations in  $\theta$  (discussed below). This discreteness should be kept in mind when interpreting all results.

**3.2.2. Rotation speed: Varying  $P$ .** Rotation also strongly affects tidal breakup since centrifugal acceleration from the asteroid's spin may directly enhance or oppose the tidal stretching. For that reason, we devote considerable effort to exploring rotation with greater range and resolution than previous studies. We have examined  $P = 4, 6, 8, 10,$  and  $12$  h for prograde rotation with no spin axis tilt, as well as the no-spin ( $P = \infty$ ) case (cases with spin axis tilt, including retrograde spin, are discussed in the next section). Figure 6 summarizes these results. The relative sizes of the plots indicate the range of  $q$ - $v_\infty$  space explored in each case. A total of 64  $q$ - $v_\infty$  pairs were sampled for each plot.

Generally, faster rotation enhances disruption, increasing the range of  $q$  and  $v_\infty$  values for which S-, B-, and M-

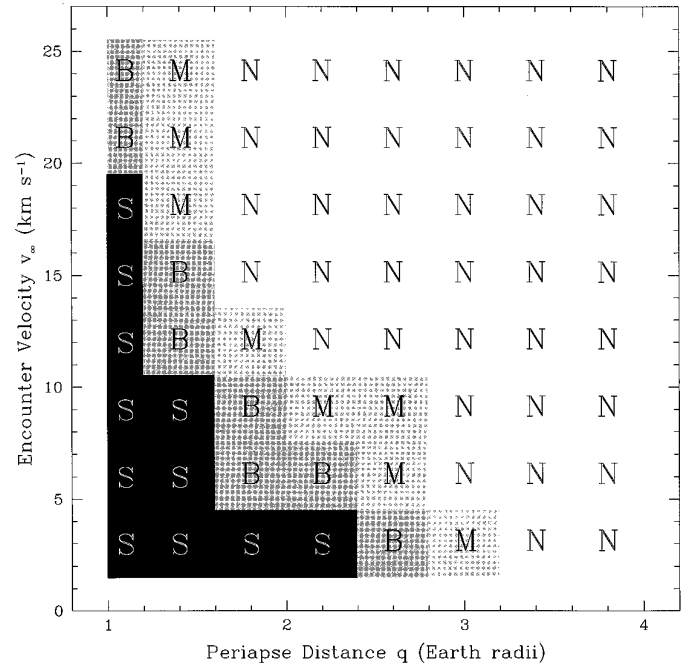


**FIG. 4.** Tidal disruption outcomes for the generic  $P = 6$  h elongated progenitor encounter with Earth as a function of close approach distance  $q$  and encounter speed  $v_\infty$ . In general, tidal disruption becomes more difficult as  $q$  and  $v_\infty$  increase.

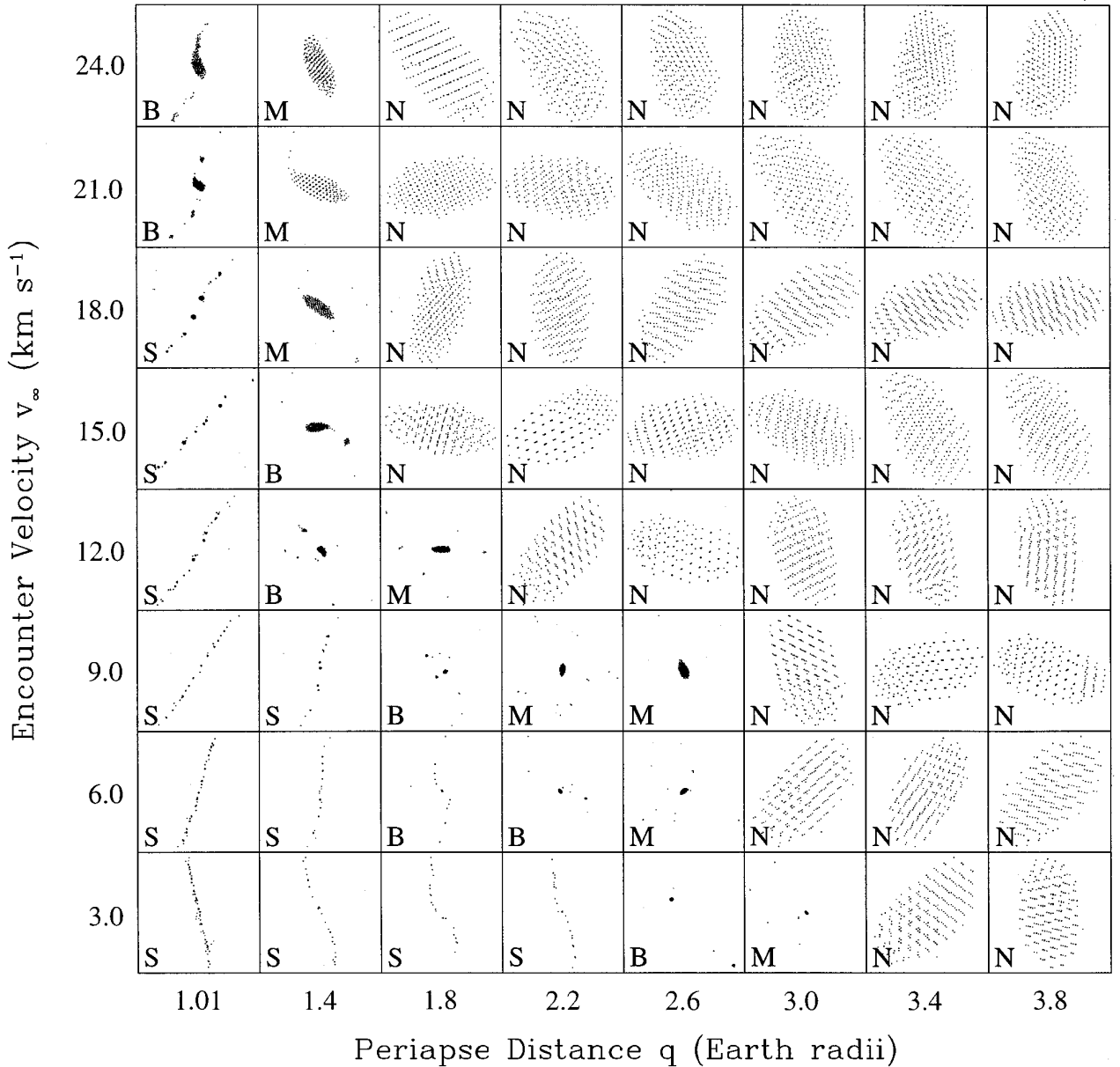


FIG. 5. A graphic illustration of the final configurations of the  $P = 6$  h Earth encounters. Each image has been scaled to fit exactly inside its box, so the N-class outcomes are zoomed views of the progenitor (2 km on a side), whereas S-class outcomes are shown in boxes as large as 650 km on a side.

class disruptions occur. Within the discreteness limits of the plots, the area encompassed by mass-loss classes shrinks as the rotation period increases. Note, however, that the difference in outcomes between  $P = 4$  h and  $P = 6$  h is greater than the difference between  $P = 10$  h and  $P = 12$  h. This effect is not surprising given the inverse square relationship of centrifugal acceleration with rotation period (cf. Eq. (1)). Since a particle at the tip of a  $P = 4$  h rubble pile moves at  $\sim 70\%$  of escape velocity, only a small increase in rotational speed from tidal forces is needed to

lift the particle into space. If the rubble pile rotated more slowly, say at  $P = 12$  h, the same particle (now moving at  $\sim 25\%$  the escape velocity) would require a bigger kick from tidal forces for ejection. Even objects without spin ( $P = \infty$ ), however, undergo tidal disruption if  $q$  and  $v_\infty$  are small enough, as seen in Fig. 6.

Generally the transitions between disruption classes in Fig. 6 follow the pattern mentioned in the previous section. That is, for each  $P$ , disruptions become milder for larger  $q$  and  $v_\infty$ . There are two notable exceptions, however:

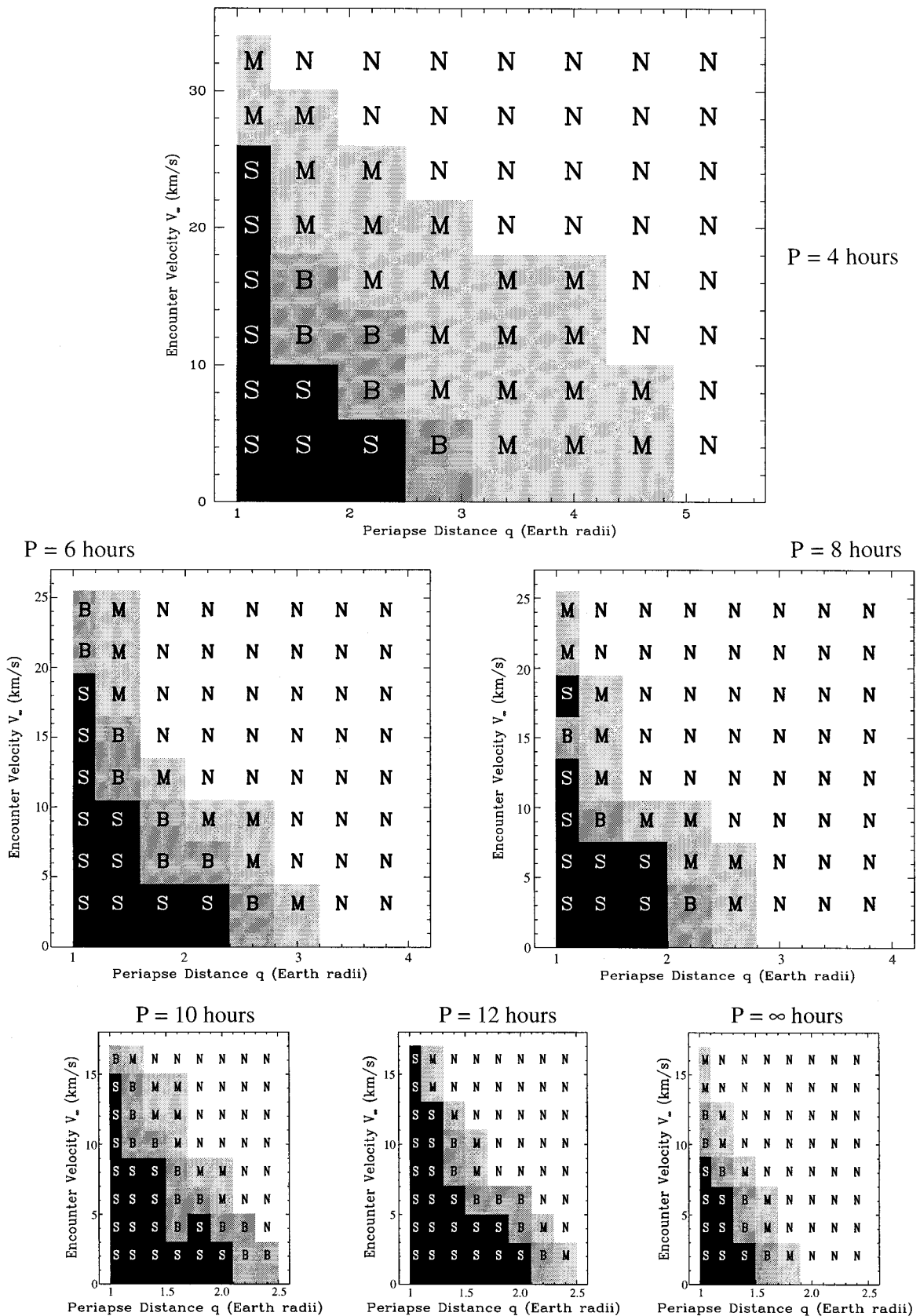


FIG. 6. Tidal disruption outcomes for elongated rubble-pile progenitors with a variety of rotation periods encountering Earth for various values of  $q$  and  $v_e$ . The plots have been scaled for easier comparison of the range of parameter space explored for each  $P$  value. The  $P = \infty$  case corresponds to zero spin.

$P = 8$  h,  $q = 1.01 R_{\oplus}$ ,  $v_{\infty} = 15$  km s<sup>-1</sup> (a B-class outcome where S-class was expected) and  $P = 10$  h,  $q = 1.6 R_{\oplus}$ ,  $v_{\infty} = 4$  km s<sup>-1</sup> (also a B-class where S-class was expected). Closer examination reveals that both these cases are examples of near perfect splitting of the progenitor asteroid. In the former case, the asteroid split into two roughly equal pieces, placing it at the border of S- and B-class disruption. In the latter case, the asteroid failed to split, but became highly elongated and ejected enough mass to put it firmly in the B-class disruption category. Runs in the vicinity of both cases exhibit similar behavior (near fission), indicating that the apparent nonconformity of these cases is simply due to our rigid mathematical definition of S- and B-class events. These marginally catastrophic disruptions may lead to the formation of double-lobed asteroids or contact binaries (see Section 4.1.5 for further discussion).

**3.2.3. Spin axis orientation: Varying  $\alpha$  and  $\beta$ .** The direction of the rubble pile’s spin axis also plays a role in tidal breakup. So far we have shown only pure prograde cases ( $\alpha = 0^\circ$ ), though retrograde ( $\alpha = 180^\circ$ ) and intermediate obliquity cases (with  $0^\circ < \alpha < 180^\circ$  and  $0^\circ \leq \beta \leq 360^\circ$ ) evidently must occur as well. Unfortunately, obliquity comprises a very large portion of parameter space. For computational expediency, we have limited our investigation of  $\alpha$  and  $\beta$  to a representative S-class event ( $P = 6$  h,  $q = 1.4 R_{\oplus}$ ,  $v_{\infty} = 6$  km s<sup>-1</sup>) and B-class event (same  $P$  and  $v_{\infty}$  but  $q = 2.2 R_{\oplus}$ ).

Figure 7 shows the effect of varying the obliquity  $\alpha$  and  $\beta$  for these cases. The rotation pole angle  $\alpha$  was varied between  $0^\circ$  and  $180^\circ$  in steps of  $30^\circ$ . The rotation axis was constrained to lie along the  $xz$  plane ( $\beta = 0^\circ$  and  $180^\circ$ ) or  $yz$  plane ( $\beta = 90^\circ$  and  $270^\circ$ ). Computational constraints prevented systematic testing of additional angle combinations, though the other values of  $\beta$  we did test yielded results between these extremes.

From Fig. 7, parameters that produce an S-class event when  $\alpha = 0^\circ$  continue to produce outcomes with strong mass loss so long as the rubble pile’s rotation is prograde (i.e.,  $\alpha \leq 90^\circ$ ). The severity of mass shedding within a class, however, decreases somewhat as  $\alpha$  approaches  $90^\circ$ . For example, the B-class event in the same figure changes to an M-class event as  $\alpha$  increases. Once rotation becomes retrograde ( $\alpha > 90^\circ$ ), mass shedding is strongly suppressed. Note that the transition is not as rapid when the rotation axis is confined to the  $yz$  plane ( $\beta = 90^\circ$  and  $270^\circ$ ). This is because the long axis of the body continues to sweep towards and away from Earth, allowing the large moment arm to assist the breakup. We also caution that these outcomes have been influenced by noise in  $\theta$  (next section): as the rotation axis moves away from the  $z$  axis,  $\theta$  becomes more difficult to measure and therefore more difficult to constrain.

We have also examined pure retrograde spin cases

( $\alpha = 180^\circ$ ) for various values of  $q$  and  $v_{\infty}$ . Our results show that rubble piles with spin period of  $P = -6$  h are nearly immune to tidal disruption, regardless of their trajectories. Milder  $P = -12$  h runs were also performed (Fig. 8; compare with Fig. 6). Although the range of disruption outcomes over  $q$  and  $v_{\infty}$  is greatly reduced compared to the prograde case, note that all four outcome classes are still seen. Slowly rotating rubble piles have relatively little angular momentum, so they are about as difficult to disrupt as objects without spin, and such  $P = \infty$  objects still show some S-class outcomes (Fig. 6).

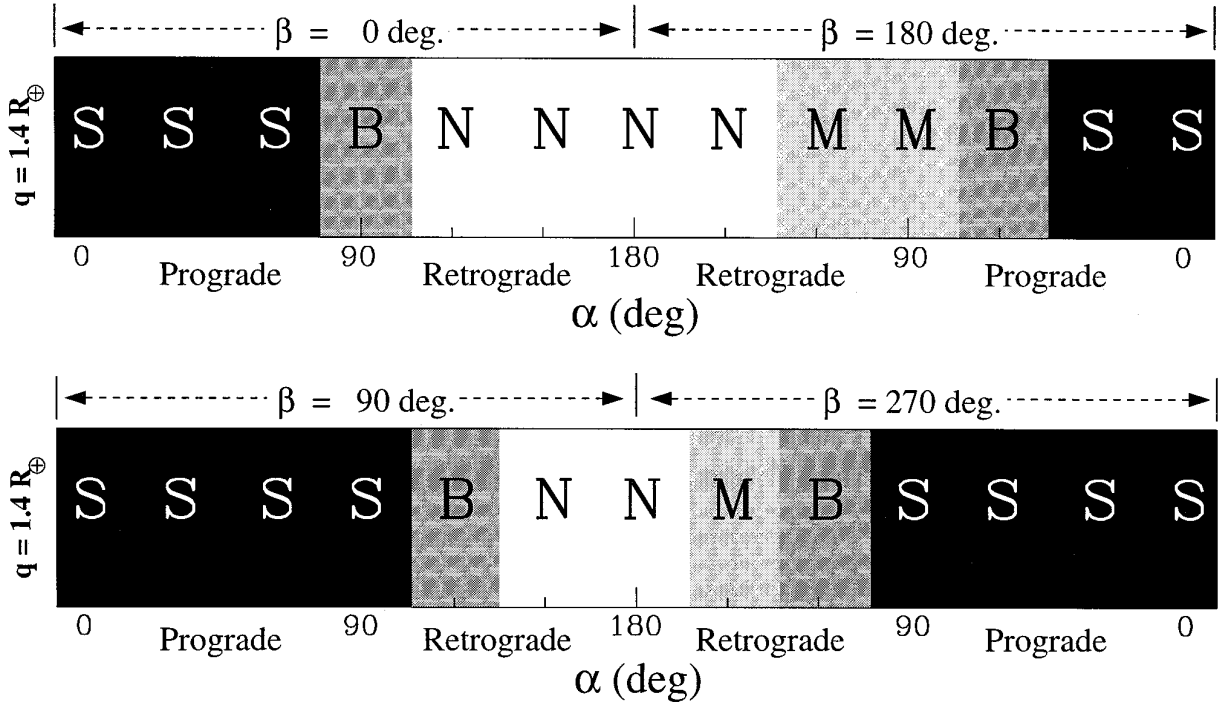
**3.2.4. Long-axis orientation: Varying  $\theta$ .** The effectiveness of tidal disruption also depends on  $\theta$ , the rotational phase of the rubble pile’s long axis at perigee. Our runs show that when the long axis is rotating toward Earth in the prograde sense ( $\alpha < 90^\circ$ ,  $0^\circ \leq \theta \leq 90^\circ$ ), tidal breakup is enhanced. When the leading long axis is rotating away from Earth ( $90^\circ \leq \theta \leq 180^\circ$ ), breakup is resisted. Recall that tidal forces near perigee stretch the shape of the equipotential surface of the body in the direction of Earth; particles move “downhill” to fill that shape if they can. When  $90^\circ \leq \theta \leq 180^\circ$ , however, this movement is opposed by the rotation, which often causes the particles to collapse back to the remnant rubble pile, typically making the shape more spherical. This is similar to what happens to a rubble pile with retrograde spin.

Since tidal disruption is preferred when  $\theta$  is between  $0^\circ$  and  $90^\circ$ , we try to “aim” the initial phase angle of the body to reach  $\theta \sim 45^\circ$ . Unfortunately it is difficult to force a particular value of  $\theta$  on a given run. The reasons for this are threefold: (1) torques applied close to perigee that depend on the orientation angle often change the rotation rate; (2) the rubble pile may contract or expand slightly as it relaxes at the start of each run, causing a minute change in the rotation period (this effect is small but can result in a noticeable phase difference after many rotations; eliminating the effect was not considered worth the additional computational expense); and (3) unavoidable but small (<5%) changes in spin rate attributable to the finite time step of the integration algorithm.

To get around these complications, we use a trial-and-error technique, throwing out runs with unfavorable  $\theta$  and reorienting the initial phase angle until a favorable  $\theta$  is achieved. The resulting variation in  $\theta$  effectively adds to the discreteness noise in the outcome plots. Typically more than 50% of runs were rejected on the first pass; subsequent passes had correspondingly lower rejection rates.

**3.2.5. Density: Going from Earth to the Moon.** As the Roche limit suggests, tidal disruption is a function of the density ratio between the primary target body (planet or moon) and the interloper, albeit one with a weak  $1/3$  power dependence. Because this parameter has been explored thoroughly by previous groups (e.g., Asphaug and Benz

**S-class event caused when  $\alpha = 0^\circ$**



**B-class event caused when  $\alpha = 0^\circ$**

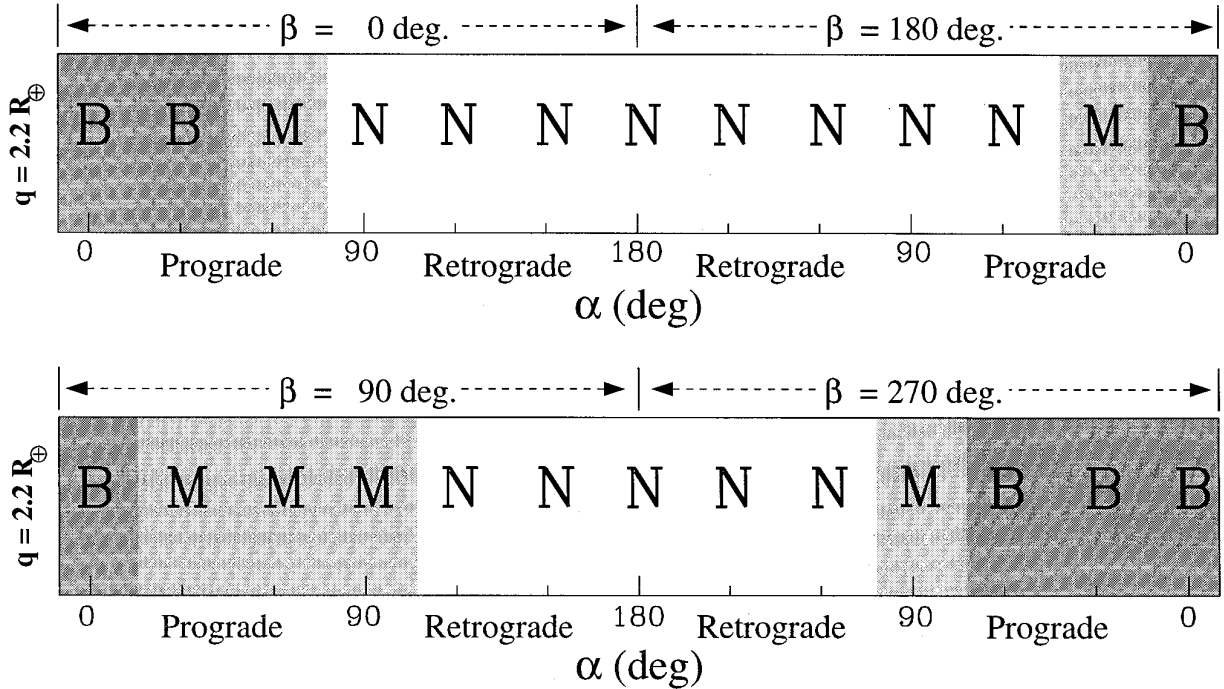


FIG. 7. This set of plots shows the effect of varying  $\alpha$  and  $\beta$  for two sets of  $P = 6$  h and  $v_\infty = 6$  km s $^{-1}$  Earth encounters, one with  $q = 1.4 R_\oplus$ , the other  $q = 2.2 R_\oplus$ . For each case, the top plot shows the effect of varying  $\alpha$  while restricting the rotation axis to the  $xz$  plane ( $\beta = 0^\circ/180^\circ$ ), while the bottom plot corresponds to  $\beta = \pm 90^\circ$  (the  $yz$  plane). For the  $q = 1.4 R_\oplus$  case, the zero-tilt outcome is S-class. As the rotation angle approaches  $90^\circ$ , the mass loss drops steeply until for  $\alpha > 90^\circ$  the outcome becomes N-class. Note that this transition is not quite as steep for  $\beta = \pm 90^\circ$  because the long axis of the asteroid continues to sweep toward and away from the planet, allowing the large moment arm to assist the breakup. The  $q = 2.2 R_\oplus$  case, though a milder disruption class, also shows this trend.

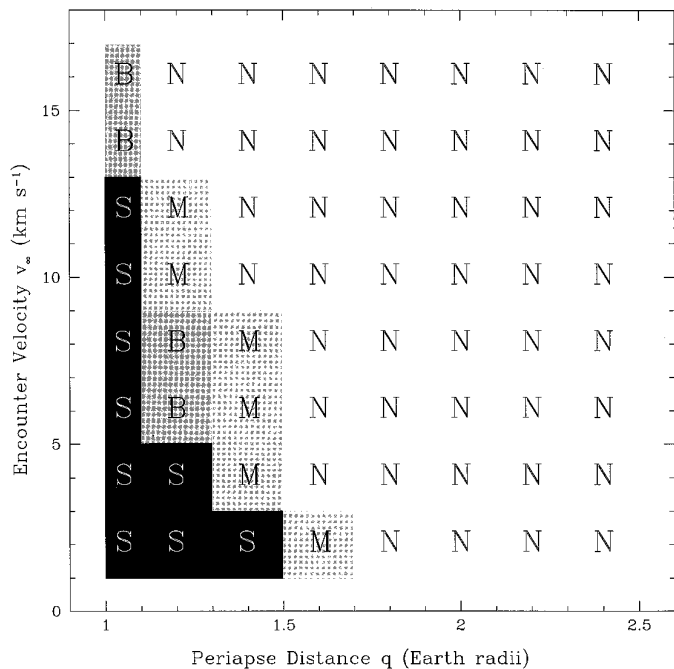


FIG. 8. Outcome plot for a retrograde  $P = -12$  h case. Compare with  $P = 12$  h and  $P = \infty$  in Fig. 6. Rubble piles with retrograde rotation are less susceptible to tidal breakup so the range of  $q$  and  $v_\infty$  for which mass loss occurs is reduced. It is still possible to get S-class outcomes, however, for small enough  $q$  and  $v_\infty$ . As the retrograde spin increases, though, the mass loss region shrinks even further.

1996), we have so far restricted ourselves to exploring tidal disruption by Earth (density  $5.5 \text{ g cm}^{-3}$ ). We now briefly explore the interesting case of tidal disruption by our Moon ( $3.3 \text{ g cm}^{-3}$ ). The results for flybys of the Moon by our rubble pile ( $P = 6 \text{ h}$ ,  $\alpha = 0$ ) are shown in Fig. 9 (compare with Fig. 4 and note change in scale).

The Moon disrupts fewer rubble piles than the Earth because of its smaller Roche sphere. Hence, for breakup to occur, an asteroid or comet must travel closer to the Moon and have a smaller encounter speed than at Earth. However, there is a minimum encounter speed,  $\sim 1.5 \text{ km s}^{-1}$ , for objects encountering the Moon, due to Earth’s proximity. Figure 9 shows that  $v_\infty$  values even slightly in excess of  $2 \text{ km s}^{-1}$  result in virtually no mass loss (recall that the mean encounter speed of ECAs with Earth is  $\sim 12 \text{ km s}^{-1}$ ). Also note that these results are for favorable values of  $\theta$ . Hence, though still possible, significant tidal disruption or distortion of ECAs is far more likely to occur in the vicinity of Earth than the Moon. These results may explain why catena-type crater chains probably do not exist on Earth (Bottke *et al.* 1997; cf. Section 4.1.2).

Finally, we note that the lunar results, even though they are somewhat affected by Earth’s gravity, suggest that disruption among smaller bodies interacting with one another

(i.e., asteroids or comets) is unlikely to occur unless both  $q$  and  $v_\infty$  are very low.

**3.2.6. Shape: Near-spherical progenitor.** To gauge how the shape of the rubble pile affects tidal disruption, we have completed many runs with our code using a near-spherical progenitor. We arranged the particles in “hexagonal close-packed” (HCP) form<sup>4</sup> with an effective packing efficiency (solid volume filling factor) of 52%.<sup>5</sup> This yielded a shape of physical dimension  $1.93 \times 1.92 \times 1.88 \text{ km}$ . The remaining parameters were similar to the elongated case. Recall, however, that the elongated progenitor was obtained by distorting a close-packed spherical progenitor. The individual particle density in each configuration was therefore adjusted to keep the bulk density the same ( $3.6 \text{ g cm}^{-3}$  for the elongated case,  $3.9 \text{ g cm}^{-3}$  for the spherical case).

Figure 10 shows the results for this rubble pile with  $P = 6 \text{ h}$  and  $\alpha = 0^\circ$ . Comparing these results with the elongated progenitor run shown in Fig. 4, we immediately see that our spherical progenitor is much more resistant to tidal disruption, with far fewer instances of S-, B-, and M-class

<sup>4</sup> HCP structures have the same density as cubic close-packed (CCP) structures, but lower symmetry. This could make a difference in resistance to distortion or disruption, an interesting area for future study.

<sup>5</sup> The effective packing efficiency is less than the maximum close-packed efficiency of 74% due to finite size effects. As the number of particles increases, the effective packing efficiency approaches this maximum value.

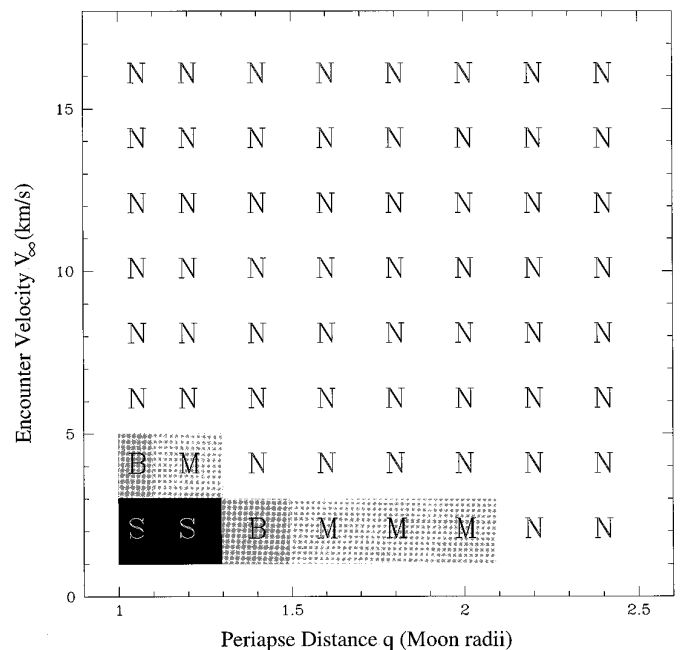


FIG. 9. Outcome plot for  $P = 6 \text{ h}$  encounters with the Moon. Compare with Fig. 4. ECAs are not likely to be disrupted by the Moon.

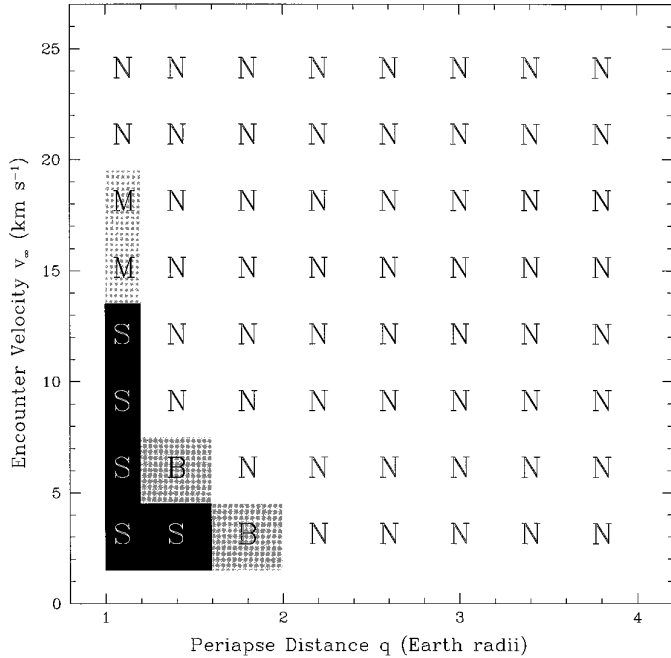


FIG. 10. Outcome plot for the nearly spherical body with  $P = 6$  h encountering Earth. Compare with Fig. 4. Note how the lower potential energy state of this object drastically reduces the disruption region.

disruptions. Indeed, except at small  $q$ , these results are only slightly more favorable for disruption than for an elongated progenitor at the Moon (Fig. 9)! Recall that spherical progenitors have lower gravitational potential energies, making them intrinsically more stable against tidal disruption than other configurations. Thus, spherical bodies, with small “moment arms,” are not subject to as great a degree of tidal stress at close approach as elongated objects with favorable alignment (i.e.,  $\theta$  between  $0^\circ$  and  $90^\circ$ ). Note that, for the near-spherical case, the orientation angle  $\theta$  at perigee has little meaning since the object is almost symmetric. Otherwise, we see the same trends with respect to  $q$ ,  $v_\infty$ , and  $P$  as for the elongated progenitor, namely that breakup is favored when these values are small.

We have also examined the effect of the spin axis orientation ( $\alpha$  and  $\beta$ ) for the near-spherical case. In all runs performed, the results show trends which are consistent with those of the elongated case, although changes in outcome seem less sensitive to variations in  $\beta$ . Hence for the near-spherical case, breakup is still favored for prograde spin ( $\alpha < 90^\circ$ ) and resisted for retrograde spin ( $\alpha > 90^\circ$ ).

To check our results, we compare our outcomes to simulations performed by Asphaug and Benz (1996) (their Fig. 14), who also used a spherical rubble pile with  $\rho = 2.0$  g  $\text{cm}^{-3}$ . However, they used a rubble pile without rotation on a parabolic trajectory ( $v_\infty = 0$  km  $\text{s}^{-1}$ ), while we used one with  $P = 6$  h prograde on hyperbolic trajectories with

$v_\infty \geq 3$  km  $\text{s}^{-1}$ . Fortunately, from what we have learned in the previous sections, we recognize that the prograde spin in our model is offset to a certain extent by the faster trajectory. Asphaug and Benz found that S-class disruptions occur when  $q \leq 1.4 R_\oplus$ , consistent with our results. Their plot also shows the Sridhar and Tremaine (1992) disruption limit at  $q \sim 1.8 R_\oplus$ ; our results show a B-class event at that distance, but N-class events further away than that. Thus, the two codes appear to give similar results.

**3.2.7. Summary.** In general, we find that rapid prograde spin and low values of  $q$  and  $v_\infty$  are needed to cause catastrophic disruptions of rubble-pile ECAs. In contrast, rapid retrograde spin dramatically reduces the severity of disruptions for a given set of  $q$  and  $v_\infty$ , as does an unfavorable orientation at perigee. This latter effect means not every asteroid that makes a close approach inside the limit given by Eq. (3) will necessarily undergo a tidal disruption. Assuming random spin and body orientations, only half of the encountering bodies will likely be rotating prograde, and of those only half are likely to have a favorable orientation at perigee. Thus, we estimate that rapidly rotating elongated rubble piles with sufficiently low  $q$  and  $v_\infty$  have roughly a 25% chance of undergoing a tidal disruption event each time they encounter Earth. Slower rotators require smaller  $q$  and  $v_\infty$  to disrupt, but slow retrograde rotators lose some of the protection against disruption noted for fast retrograde rotation. These results are used in Section 4.1 to estimate the rate and consequences of tidal disruption near Earth.

### 3.3. Discussion

As we have shown, tidal disruption ejects fragments of many sizes from the progenitor, often leaving the remnant with an unusual shape and a new rotation period. Table I provides data for more quantitative analysis of the generic  $P = 6$  h Earth encounter (Fig. 4). Similar tables are available on request to the authors for the other runs discussed in this paper. In the table,  $q$ ,  $v_\infty$ , and  $\theta$  have the usual definitions; “C” is the outcome class;  $P_{\text{rem}}$ ,  $\epsilon_{\text{rem}}$ , and  $M_{\text{rem}}$  are the rotation period, “ellipticity,” and mass fraction, respectively, of the remnant (cf. Section 2.4.2);  $M_{\text{acc}}$ ,  $M_{\text{orb}}$ , and  $M_{\text{esc}}$  are the mass fraction of material accreting, orbiting, and escaping the remnant, respectively (Section 2.4.4; note  $M_{\text{rem}} + M_{\text{acc}} + M_{\text{orb}} + M_{\text{esc}} \equiv 1$ ); and  $\delta R$  is a clump size-distribution statistic, defined below. Runs with  $\theta < 25^\circ$  or  $\theta > 65^\circ$  in the Notes column should not be considered representative of the maximum disruption state for that choice of parameters because of the marginal  $\theta$  values.

**3.3.1. Ejecta statistics.** For the S-class outcomes, the average  $M_{\text{acc}}/M_{\text{orb}}/M_{\text{esc}}$  values are 0.008/0.075/0.629, respectively, while the mean remnant mass fraction,  $\overline{M}_{\text{rem}}$ , is 0.288. There are on average 10.5 clumps created in each

TABLE I  
Results for the  $P = 6$  h Elongated Progenitor Encountering Earth

$q$	$v_\infty$	$\theta$	$C$	$P_{\text{rem}}$	$\epsilon_{\text{rem}}$	$M_{\text{rem}}$	$M_{\text{acc}}$	$M_{\text{orb}}$	$M_{\text{esc}}$	$\delta R$	Notes
1.0	3	44	S	-7.5	0.15	0.105		0.008	0.887	0.18	
1.0	6	50	S	4.5	0.45	0.146			0.854	0.34	
1.0	9	44	S	7.1	0.28	0.146		0.004	0.851	0.25	
1.0	12	64	S	7.5	0.18	0.312	0.081	0.008	0.599	0.39	
1.0	15	26	S	7.6	0.13	0.287	0.004	0.004	0.704	0.28	
1.0	18	50	S	6.4	0.19	0.377		0.437	0.186	0.40	
1.0	21	53	B	4.9	0.43	0.785	0.158	0.008	0.049	0.51	
1.0	24	40	B	6.7	0.58	0.785	0.154	0.049	0.012	0.56	
1.4	3	64	S	4.6	0.55	0.267		0.008	0.725	0.47	
1.4	6	37	S	4.7	0.18	0.251		0.012	0.737	0.35	Fig. 2
1.4	9	38	S	5.7	0.22	0.348		0.077	0.575	0.35	
1.4	12	69	B	5.1	0.44	0.850		0.024	0.125	0.79	$\theta > 65^\circ$
1.4	15	37	B	5.0	0.64	0.883	0.105	0.008	0.004	0.73	
1.4	18	51	M	5.3	0.65	0.968		0.024	0.008	1.06	
1.4	21	54	M	4.5	0.62	0.988			0.012		
1.4	24	40	M	4.8	0.59	0.996			0.004		
1.8	3	60	S	4.8	0.25	0.437		0.263	0.300	0.46	
1.8	6	55	B	5.0	0.55	0.725		0.032	0.243	0.80	Fig. 12a
1.8	9	34	B	5.1	0.32	0.696		0.275	0.028	0.34	
1.8	12	59	M	5.5	0.57	0.935		0.032	0.032	0.94	
1.8	15	21	N	4.4	0.51	1					$\theta < 25^\circ$
1.8	18	51	N	4.3	0.52	1					
1.8	21	53	N	4.3	0.49	1					
1.8	24	39	N	4.6	0.51	1					
2.2	3	26	S	4.3	0.23	0.494		0.004	0.502	0.36	
2.2	6	26	B	4.4	0.44	0.870		0.117	0.012	0.65	Fig. 2
2.2	9	32	M	4.8	0.54	0.939		0.016	0.045	0.77	Fig. 2
2.2	12	61	N	3.9	0.50	1					
2.2	15	35	N	4.1	0.47	1					
2.2	18	52	N	4.1	0.44	1					
2.2	21	57	N	4.2	0.41	1					
2.2	24	40	N	4.5	0.44	1					
2.6	3	36	B	4.5	0.24	0.798			0.202	0.33	
2.6	6	44	M	4.3	0.54	0.955		0.024	0.020	0.84	
2.6	9	31	M	4.0	0.54	0.996		0.004			
2.6	12	63	N	4.0	0.42	1					
2.6	15	35	N	4.2	0.43	1					
2.6	18	53	N	4.4	0.44	1					
2.6	21	56	N	4.6	0.42	1					
2.6	24	42	N	4.7	0.43	1					
3.0	3	45	M	4.0	0.51	0.964		0.012	0.024	1.02	
3.0	6	21	N	3.8	0.43	1					$\theta < 25^\circ$
3.0	9	31	N	3.9	0.43	1					
3.0	12	66	N	4.3	0.42	1					$\theta > 65^\circ$
3.0	15	34	N	4.5	0.43	1					
3.0	18	53	N	4.6	0.43	1					
3.0	21	57	N	4.9	0.42	1					
3.0	24	40	N	4.9	0.43	1					
3.4	3	68	N	3.8	0.44	1					$\theta > 65^\circ$
3.4	6	40	N	3.8	0.44	1					
3.4	9	23	N	4.3	0.42	1					$\theta < 25^\circ$
3.4	12	55	N	4.4	0.43	1					
3.4	15	54	N	4.6	0.43	1					
3.4	18	53	N	4.8	0.43	1					
3.4	21	57	N	4.9	0.43	1					
3.4	24	41	N	5.0	0.43	1					
3.8	3	66	N	4.0	0.41	1					$\theta > 65^\circ$
3.8	6	20	N	4.3	0.41	1					$\theta < 25^\circ$
3.8	9	28	N	4.4	0.43	1					
3.8	12	51	N	4.5	0.43	1					
3.8	15	35	N	4.8	0.43	1					
3.8	18	53	N	4.9	0.42	1					
3.8	21	57	N	5.1	0.42	1					
3.8	24	41	N	5.1	0.42	1					

of these events (recall that a clump is a fragment containing three or more individual particles; cf. Section 2.4.1), with each clump accounting for  $\sim 6.6\%$  of the mass of the original progenitor (i.e., a fractional mass of 0.066 each). The statistics for all 78 S-class events seen in Fig. 6 taken as a whole were similar: mean ejecta fractional masses of 0.023/0.048/0.681,  $\overline{M}_{\text{rem}} = 0.247$ , and 10.8 clumps created per event, with an average mass fraction of 0.068 each. Individual particles were also stripped away, but they were found to comprise 1% or less of the progenitor's mass.

The size distribution of the S-class clumps is difficult to determine reliably without more particles to improve the resolution. A crude quantitative measure is given in Table I by  $\delta R$ , the ratio of the standard deviation of the sizes of all clumps in the outcome to the size of the largest remnant. Values of  $\delta R$  near zero imply uniformity (values of exactly zero generally mean no clumps were stripped from the progenitor; for these cases the entry under  $\delta R$  is blank). Our results show that S-class events cover a wide range of  $\delta R$  values but generally have  $\delta R < 0.5$  (mean 0.35). For example, the first run listed in the table produced 20 similarly sized clumps, yielding a  $\delta R$  value of 0.18, whereas less-energetic disruptions tended to generate fewer, less-uniform clumps, yielding larger  $\delta R$  values (see Fig. 5, though the differences are difficult to discern by eye).

The B-class outcomes in Table I yield similar mean  $M_{\text{acc}}$  and  $M_{\text{orb}}$  ratios to those of S-class outcomes, but far smaller mean  $M_{\text{esc}}$  values: 0.052/0.064/0.084, with  $\overline{M}_{\text{rem}} = 0.799$ . Here, only 2.5 clumps on average are created per event, each with an average mass fraction of 0.074. Thus, fewer clumps are shed, but the clumps themselves are roughly the same size on average as those formed in S-class events. For the 42 B-class events found in Fig. 6 taken as a whole, the results are again similar: ejecta mass fractions 0.039/0.064/0.126,  $\overline{M}_{\text{rem}} = 0.771$ , 3.5 clumps of fractional mass 0.059 each created per event. The remaining ejecta are predominantly individual particles; roughly 4 are shed during each event. They still constitute only a small mass fraction. The average  $\delta R$  value for the B-class events shown in Table I is 0.59, larger than for any S-class event. This increase indicates that B-class ejecta are less uniform than the S-class clumps seen previously.

Marginal S-class/B-class disruptions often produce two or three big components which are close to one another. Examples of this include the S-class  $q = 2.2 R_{\oplus}$ ,  $v_{\infty} = 3 \text{ km s}^{-1}$  outcome and the B-class  $q = 2.6 R_{\oplus}$ ,  $v_{\infty} = 3 \text{ km s}^{-1}$  outcome in the table (both have relatively low  $\delta R$  values); Fig. 5 indicates that they are practically fission events. Comparable fission events are observed when the spin-axis- or long-axis-orientation angles differ from their nominal values ( $\alpha = 0^\circ$ ;  $\theta \sim 45^\circ$ ) in what would otherwise be a typical S-class disruption. Though we have not yet completed enough runs to do a quantitative study, we hypothesize that some of the double-lobed shapes seen

among the Earth-crossing asteroids (e.g., 4769 Castalia, 2063 Bacchus) may have been produced by these fission-type events (Section 4.1.5).

Mild M-class disruptions, by definition, shed little material. For this reason, the results for these cases must be interpreted with caution, since the resolution of our rubble pile was probably too coarse to detect marginal mass loss or clump formation. The ejecta mass fractions for the M-class disruptions in Table I are 0.000/0.014/0.018, with  $\overline{M}_{\text{rem}} = 0.968$ . A single clump containing 3 or 4 particles was created about 60% of the time (5 cases out of 8). Results for all 64 M-class events in Fig. 6 follow a similar trend: 0.006/0.014/0.017,  $\overline{M}_{\text{rem}} = 0.963$ , with a single small clump ejected about 45% of the time. Ejected single particles (or groups of two particles) were found to be relatively more important in these mild disruption cases. M-class events shed, on average, 5 unclumped particles per event, though the range can vary widely. In one case reported in Table I, the progenitor expelled 10 particles, while in a second case, only a single particle was lost. For these cases,  $\delta R$  is not a particularly meaningful statistic, but the average value for the clump-shedding M-class outcomes shown in Table I is 0.58.

In summary, we find two broad types of ejecta size distributions: (1) an SL9-type distribution of several similar-sized fragments and scattered smaller fragments; and (2) mass-shedding events producing small clumps and fragments.

*3.3.2. Orbital parameters of bound ejecta.* Although the bulk of all shed material ultimately escapes the remnant rubble pile, a nonetheless-significant amount remains in orbit around the progenitor (10% of all the material averaged over all disruptive outcomes in Fig. 6). Thus, tidal disruption seems capable of creating binary asteroids (Bottke and Melosh 1996a,b; cf. Section 4.1.3).

At least 23 of the 27 S-, B-, and M-class events in Table I place clumps or single particles into bound orbits. This number might be even higher, since we only consider bound orbits around the remnant rubble pile; S-class events may create multiple binary systems. On average, each disruption places two fragments (clumps or single particles) into orbit.

The median semimajor axis among all 47 orbiting fragments found in the Table I runs is 6.2 km. The mean is much higher (56 km, with standard deviation  $\sigma = 249 \text{ km}$ ) since 4 fragments were thrown out to  $a = 138\text{--}1680 \text{ km}$ . The median eccentricity for the 47 bodies is 0.77, with the mean slightly smaller (0.73,  $\sigma = 0.20$ ). The median periape (2.0 km) is small enough that a number of these orbits are probably unstable.

Finally, the median inclination of these bodies is  $7.2^\circ$ , with the average slightly higher ( $12.3^\circ$ ,  $\sigma = 18.3^\circ$ ). These low values are not surprising, given that most particles are

stripped off in the rubble pile’s equatorial plane during these simulations. Preliminary investigation of the inclination distribution for cases with spin-axis tilt shows more complex behavior that warrants future study.

**3.3.3. Spin and shape changes.** The  $P_{\text{rem}}$  and  $\varepsilon_{\text{rem}}$  columns of Table I show the effect of tidal disruption on progenitor spin and shape. In each case the remnant is stable against rotational disruption, as defined by Eq. (1) (where we have taken  $a/b = 1/(1 - \varepsilon_{\text{rem}})$  by invoking the approximation  $a = a_1$ ,  $b = \frac{1}{2}(a_2 + a_3)$  and assuming that the bulk density of the remnant remains largely unchanged). For example, a body with a density of  $2 \text{ g cm}^{-3}$  and  $P = 3.5, 4.0, 4.5, 5.0, 5.5,$  and  $6.0 \text{ h}$  sheds mass when  $\varepsilon_{\text{rem}} = 0.56, 0.66, 0.73, 0.78, 0.82,$  and  $0.85$ . Thus none of the remnants in Table I are in danger of flying apart from rotation alone. Note that the elongated progenitor rubble pile, with  $\varepsilon_{\text{rem}} = 0.43$ , is also stable for the spin periods tested. The nearly spherical rubble pile, with  $\varepsilon_{\text{rem}} = 0.02$ , is rotationally stable for all  $P \gtrsim 2.3 \text{ h}$ .

We find that most S- and some B-class events are so destructive that the spin and ellipticity of the remnant are only mildly correlated with the progenitor values. For S-class events, gravitational instabilities cause particles to agglomerate after the disruption, leaving behind near-spherical clumps whose final spins are essentially random. For B-class events, large clumps stripped away from the rubble pile may also leave behind more spherical remnants.

Many B- and M-class events, however, can cause substantial  $\varepsilon_{\text{rem}}$  increases since tidal forces are only strong enough to elongate the progenitor and strip small amounts of mass from the ends. The most extreme example in the table (also see Fig. 5) has  $\varepsilon_{\text{rem}} = 0.65$  for the M-class  $q = 1.4 R_{\oplus}$ ,  $v_{\infty} = 18 \text{ km s}^{-1}$  encounter. Ellipticities as high as 0.69 have been noted in other runs. The spin rate only increases by a small amount, though, as the stretching of the body opposes the spin-up effect of the tidal torque.

Finally, as the outcomes become even less destructive (weak M- and nondisruptive N-class), the values of  $\varepsilon_{\text{rem}}$  only marginally increase. Spin rates, on the other hand, can still increase considerably, even for large  $q$  encounters. For example, the N-class event for  $q = 3.8 R_{\oplus}$ ,  $v_{\infty} = 12 \text{ km s}^{-1}$  shows a decrease in  $P$  from 6 to 4.5 h. If succeeding encounters were prograde, therefore, the object would be much more likely to disrupt.

Another observation (not shown in the table) is that retrograde encounters generally reduce the rubble pile’s ellipticity, sometimes to near zero (values as low as 0.05 were noted for some  $P = -12 \text{ h}$  cases, from a starting value of 0.43). In these cases the rubble pile is pulled apart only slightly at perigee and then recollapses to a lower energy state. Each particle of a retrograde rotator passes the sub-Earth point faster than those of a prograde rotator would, so the tidal acceleration has less time to build up.

The final rotation period  $P_{\text{rem}}$  depends on the size of the torque relative to the magnitude of rotational inertia in the system. For example, a  $P = -12 \text{ h}$  test body that experienced strong torque ( $q = 1.4 R_{\oplus}$  and  $v_{\infty} = 12 \text{ km s}^{-1}$ ) had its spin reversed ( $P_{\text{rem}} = +10.3 \text{ h}$ ) and had its ellipticity strongly reduced ( $\varepsilon_{\text{rem}} = 0.11$ ). On the other hand, a test body subjected to weak torque ( $q = 2.2 R_{\oplus}$ ,  $v_{\infty} = 12 \text{ km s}^{-1}$ ;  $P$  still  $-12 \text{ h}$ ) experienced far less change in spin and ellipticity ( $P_{\text{rem}} = -10.5 \text{ h}$ ,  $\varepsilon_{\text{rem}} = 0.35$ ). In this case the slight increase in retrograde spin correlates well with the mild contraction of the body, indicating that the tidal torque had little effect.

Shape and spin changes are similarly dependent on the orientation of the phase angle  $\theta$ , with angles between  $0^\circ$  and  $90^\circ$  providing maximum effects (Section 3.2.4). This result holds even for retrograde encounters: one run with  $q = 1.4 R_{\oplus}$ ,  $v_{\infty} = 6 \text{ km s}^{-1}$ ,  $P = -6 \text{ h}$ , and  $\theta = 58^\circ$  had  $P$  increase to  $+5.4 \text{ h}$ , while a second run with the same orbital parameters and  $\theta = 141^\circ$  had  $P$  increase from  $-6$  to  $+6.9 \text{ h}$ . In both cases, the rubble pile ended up nearly spherical.

**3.3.4. Long-term evolution.** The evolution of the rubble pile and any shed fragments is not necessarily completed by the end of the simulation. Recall that  $M_{\text{rem}}$  alone defines the outcome class (Section 2.4.2); we do not add the mass fraction  $M_{\text{acc}}$  to  $M_{\text{rem}}$ , even though it could potentially change the outcome class. This is unlikely for most of the runs in Fig. 6, however, since most ejecta move on escape trajectories. Nevertheless, as a check we integrated a few representative cases over 10 times the initial time interval. Our results indicate no changes in outcome class, but some minor changes to the remnant rubble pile properties do occur as material is reagglomerated. Further work needs to be done to study the long-term evolution of these models.

## 4. CONCLUSIONS

### 4.1. Applications

Starting from the premise that Earth-crossing asteroids are intrinsically weak rubble piles, our simulations may explain some unusual phenomena in the terrestrial-planet region. It seems that planetary tides play a much larger role in the evolution of near-Earth asteroids than previously thought.

**4.1.1. Tidal disruption rates near Earth.** To gauge the effectiveness and importance of tidal disruption in the terrestrial-planet region, we can estimate the frequency of S-, B-, and M-class events near Earth and Venus from our map of tidal disruption outcomes as a function of  $P$ ,  $q$ ,  $v_{\infty}$ ,  $\alpha$ ,  $\beta$ , and  $\theta$ . Since our sister planet is nearly as effective as the Earth at tidal disruption, we will assume that it follows the same disruption map as Earth. We also require estimates of the following quantities: (a) encounter probability of ECAs with Earth and Venus; (b) probability distribution

of ECA encounter velocities with the Earth and Venus; (c) probability distribution of rotation periods among ECAs; and (d) size–frequency distribution of (rubble-pile) asteroids in the ECA population.

These components and the method for incorporating them into the calculation are based on those described in Bottke *et al.* (1997). For brevity's sake, we only briefly summarize their method and parameter choices here. The value of (a), the average intrinsic encounter probability, was found to be  $\langle P_i \rangle = 1.12 \times 10^{-16} \text{ km}^{-2} \text{ year}^{-1}$  for Earth and  $\langle P_i \rangle = 2.02 \times 10^{-16} \text{ km}^{-2} \text{ year}^{-1}$  for Venus (calculation details in Bottke *et al.* 1994a,b). The value for Venus is somewhat higher than that for Earth, but only 40% of the known ECA population currently cross the orbit of Venus. The average encounter velocity value for the distribution described in (b) is  $\langle v_\infty \rangle = 12.47 \text{ km s}^{-1}$  for Earth and  $17.95 \text{ km s}^{-1}$  for Venus (Bottke *et al.* 1994a,b). For (c), we assumed that 80% of the ECAs have rotation periods that can be approximated as a Maxwellian with a mean period of 6 h truncated at 3.1 h (A. Harris 1996, pers. commun.); the remaining 20% were considered extremely slow rotators (e.g., 4179 Toutatis; Hudson and Ostro 1995). Finally, for (d), we assumed that approximately 40,000 ECAs have diameters larger than 250 m (Morrison 1992) with an uncertainty factor of 2; this is the minimum size for catastrophic disruptions to be controlled by the self-gravity of the target rather than its physical strength (Love and Ahrens 1996). To be conservative, our calculations often assume that rubble piles must be 1 km in diameter or larger; Morrison (1992) estimates there are 2100 such bodies that cross the orbit of Earth.

By combining (and integrating) our tidal disruption map with (a), (b), and (c), we can estimate the approximate lifetimes of rubble-pile ECAs against tidal disruption. Note that our results are slightly different than those of Bottke *et al.* (1997), who did not include Venus in the calculation nor the  $P = -12 \text{ h}$  and  $P = \infty$  runs which we incorporate here. Given that retrograde rubble piles become increasingly more difficult to disrupt as their spin rate increases, and that no mass loss is seen for  $P = -6 \text{ h}$ , we assume that tidal disruption terminates at  $P \sim -9 \text{ h}$ .

Our results indicate that the lifetime of rubble-pile ECAs against S-class events is 340 Myr, the lifetime against S- or B-class events is 190 Myr, and the lifetime against S-, B-, and M-class events is 65 Myr. Applying this lifetime to the estimated number of kilometer-sized ECAs, we find that S-class events occur near Earth (and Venus) once every 160,000 years, S- and B-events once every 90,000 years, and S-, B-, and M-events once every 31,000 years.

Bottke *et al.* (1997) also estimated the total mass shed by ECAs over time, assuming that all rubble piles are 250 m in diameter. Updating their estimate, we find that roughly  $8 \times 10^7 \text{ kg}$  of material is lost per year. We believe that it is premature to predict the size-frequency distribu-

tion of material shed, especially given the limited coverage of  $\alpha$  in our map. We can say, however, that if all this ejected material were in the form of 50-m bodies, it would be equivalent to the annual injection rate of similarly sized fragments into the 3:1 or  $\nu_6$  resonances (Menichella *et al.* 1996).

*4.1.2. Crater chain formation on the Moon from rubble-pile fragments.* As described in the Introduction, some catena-type crater chains on the Moon are thought to be formed via S-class disruption of rubble-pile asteroids or comets. In this scenario, the fragment train hits the Moon soon after being disrupted near Earth and before the train has stretched so far that it can no longer produce a recognizable crater chain on impact. Possible lunar catenae include the Davy chain, which is 47 km long and contains 23 craters, each 1–3 km in diameter, and the Abulfeda chain, which is 200–260 km long and has 24 craters, each 5–13 km in diameter (Melosh and Whitaker 1994, Wichman and Wood 1995, Schenk *et al.* 1996). Chains formed by this mechanism can be discriminated from those produced by secondary ejecta, since the latter are radially aligned with the source crater, can be associated with other secondary features, and have a distinctive morphology (e.g., “herringbone” patterns). Note that studies have shown that rubble-pile clumps, despite being intrinsically weak objects, can nonetheless produce well-defined craters on impact (e.g., Schultz and Gault 1985, Melosh 1989, Love *et al.* 1995).

Bottke *et al.* (1997) examined whether km-sized ECAs undergoing S-class disruption near the Earth could make lunar crater chains. They found that enough objects have undergone S-class disruption near Earth over the past 3.8 Gyr to account for  $\sim 1$  crater chain on the Moon, consistent with observations. Given that the Moon is a small target far from Earth, this match suggests that tidal disruption near Earth may be common.

Bottke *et al.* (1997) also investigated whether analogous S-class events near the Moon could make terrestrial crater chains, primarily in response to qualified reports of two such chains  $\leq 360 \text{ Myr}$  old by Rampino and Volk (1996) and Ocampo and Pope (1996). Bottke *et al.* (1997) found that the number of chains expected to be formed on Earth over this time was only 0.001, making the formation of terrestrial crater chains by this mechanism highly improbable.

As a related aside, we present a semi-analytical derivation of the ratio of the production rate of crater chains on the Moon to that on Earth in Appendix B. It shows that the lunar production rate is  $\sim 10$  times the terrestrial rate. Thus, if there is a single crater chain on Earth less than 360 Myr old, roughly 10 young, fresh crater chains should be found on the Moon's near side. No such chains have been observed.

*4.1.3. Formation of binary asteroids and doublet craters.* At least 3 of the 28 largest known impact craters on Earth and a similar fraction of all impact structures on Venus are doublets, formed by the nearly simultaneous impact of objects of comparable size (Bottke and Melosh 1996a,b). Mars also has doublet craters, though the fraction found there is smaller (2–3%) (Melosh *et al.* 1996). These craters are too large and too far separated to have been formed by tidal disruption just prior to impact or from asteroid fragments dispersed by aerodynamic forces during entry. Based on this fact, Melosh and Stansberry (1991) argued for formation by a population of binary asteroids.

As mentioned in the Introduction, Bottke and Melosh (1996a,b) found that the components of “contact binaries” (a crude but computationally cheap approximation to a rubble pile) can be pulled apart but remain gravitationally bound to one another, evolving into a stable binary system. They hypothesized that more complicated systems with several satellites (i.e., from tidally disrupted rubble piles) would evolve like a multiple star system, with the most stable endstate being a binary system. Such a binary could hit a planet during a later pass, creating two distinct craters (note that this explains why triplet or even quadruplet craters are not seen, since the corresponding orbital systems are intrinsically unstable). Their numerical results suggest that ~15% of all Earth-crossing asteroids (and <5% of solely Mars-crossers) evolve into binary asteroids with well-separated components. Folding these results into another model treating impact encounters between binary asteroids and a given planet, they found that they could duplicate the observed fraction of doublet craters on Earth, Venus, and Mars.

Our results, using a more sophisticated code and rubble-pile progenitor, confirm these ideas. Our runs indicate that at least 76% of all S-, B-, and M-class events produced fragments that were at least initially gravitationally bound to the remnant progenitor. As before, this value could be higher, since, for S-class events, we only consider bound orbits around the largest aggregate. In general, the bound fragments were small clumps or individual particles. Some S-class events, however, show clumps of nearly equal size orbiting one another. Such events may be responsible for doublet craters with nearly equal size components (e.g., East and West Clearwater Lake in Canada). The dynamical lifetime of ECAs against planetary collision, catastrophic collision with another asteroid, or ejection by Jupiter perturbations is thought to be on the order of 10 Myr (Milani *et al.* 1989, Michel *et al.* 1996, Gladman *et al.* 1997). Since our previous calculation showed that the lifetime of a kilometer-sized body against S-, B-, and M-class events is 65 Myr, we predict that ~15% of the ECA population are binary asteroids, almost exactly the value found by Bottke and Melosh (1996a,b).

*4.1.4. ECAs with satellites: An examination of 3671 Dionysus.* Pravec and Hahn (1997) and Mottola and Hahn (1997) claim to have discovered satellites orbiting Earth-crossing asteroids 1994 AW<sub>1</sub> and 3671 Dionysus, respectively. These claims are based on periodic dips in each asteroid’s lightcurve, interpreted as stemming from eclipses due to orbiting companions. In the case of Dionysus, however, future eclipse events were both predicted and then confirmed by other observers, mitigating the possibility that they were produced by anomalous features in the lightcurve.

Since both objects have parameters which make them likely candidates for tidal disruption, we believe that this mechanism created the alleged satellites. For example, 3671 Dionysus is slightly elongated ( $1.3 \times 1.0$  km; G. Hahn 1997, pers. commun.) and has orbital parameters  $a = 2.19$  AU,  $e = 0.54$ ,  $i = 13.6^\circ$ . From Bottke *et al.* (1994a,b) its intrinsic collision probability  $P_i$  with Earth is  $40.5 \times 10^{-18}$  km<sup>-2</sup> year<sup>-1</sup> and its average  $v_\infty$  is 10.9 km s<sup>-1</sup>. Neither value is exceptional: the collisional lifetime of Dionysus with Earth (295 Myr) is nearly twice as long as the mean of the ECA population, while its average  $v_\infty$  is only slightly below the mean ECA value (Bottke *et al.* 1994b). The spin rate of Dionysus, however, is so fast ( $P = 2.7$  h) that the object is close to the rotational disruption limit (Eq. (1)). We have not performed any runs with  $P = 2.7$  h, but as an approximation we can apply our  $P = 4$  h results to the problem. Assuming from Fig. 6 that tidal disruption occurs if Dionysus passes within  $\sim 5 R_\oplus$  of Earth at  $v_\infty = 9$  km s<sup>-1</sup>, and that its nearly spherical shape means we can neglect the effect of  $\theta$ , we estimate that its lifetime against tidal disruption is between 20 and 40 Myr, 7.5–15 times smaller than its collision lifetime. Given the range of possible outcomes seen in our results, there is a distinct possibility that this object’s satellite and its fast rotation rate may be a by-product of tidal disruption.

We recommend that observers searching for binaries among the ECAs look for the following parameters: (1) low encounter velocities with Earth or Venus; (2) high  $P_i$  values; (3) fast rotation rates; and (4) elongated shapes. Note that (1) and (2) are produced when ECAs have low inclinations ( $i$ ) and/or when they have perigees ( $q$ ) or apogeos ( $Q$ ) near Venus (0.7 AU) or Earth (1 AU).

*4.1.5. ECAs with irregular shapes: An examination of 1620 Geographos and double-lobed bodies.* Recent delay-Doppler radar studies have revealed the shapes of several ECAs (Ostro 1993). A large fraction of this set have unusual shapes which may be consistent with reshaping by planetary tides (Solem and Hills 1996). For example, 1620 Geographos ( $a = 1.25$  AU,  $e = 0.336$ ,  $i = 13.3^\circ$ ) is one of the most elongated objects known in the Solar System ( $5.11 \times 1.85$  km; Ostro *et al.* 1995a). Assuming that the minor axes have roughly the same dimension, Geographos

has an ellipticity of  $\varepsilon = 0.64$ . This shape prompted Solem and Hills (1996) to suggest that Geographos may have been reshaped by tides.

Bottke *et al.* (1998b) further investigated this idea using the model described in this paper. The distinctive morphological characteristics of Geographos, apart from its elongation, include a well-defined convex side, tapered ends, and small cusps swept back against the rotation direction much like a “pinwheel” (Ostro *et al.* 1996 and Fig. 11). In addition, the rotation period of Geographos is short (5.22 h), such that the ends are not far from the rotational disruption limit (Eq. 1). These features are diagnostic of a body that has undergone a B- or M-class disruption, particularly like those in Table I for which  $\varepsilon_{\text{rem}} > 0.60$ . In many cases, the new distorted shape is influenced by the rubble pile’s granular nature, allowing particles to leak more readily off one end than the other. The end that shed more mass frequently becomes elongated, tapered, and narrow when compared to the stubbier antipode. In addition, tidal forces stretch one side like a bow, giving the final shape a “porpoise-like” appearance. The observed cusps are remnants of material lifted off the tips and swept backward in the rubble pile’s equatorial plane.

We found that 27 of the 117 B- and M-class outcomes displayed in Fig. 6 and Fig. 8 ( $\sim 23\%$ ) have  $\varepsilon_{\text{rem}} \geq 0.60$ , suggesting that elongated shapes are common by-products. In addition, many of these remnants had one or more features reminiscent of those seen on Geographos (tapered ends, cusps, single convex side, etc.). The median rotation period for these 27 events was 5.2 h, the same as for Geographos. Thus, Bottke *et al.* (1998b) concluded that Geographos may be a tidally distorted object.

Similarly, the next most elongated asteroid, 433 Eros, may also have been reshaped by tides (Bottke *et al.* 1998b). Like Geographos, Eros has a short rotation period (5.27 h; McFadden *et al.* 1989), a large axis ratio ( $36 \times 15 \times 13$  km, or  $2.77 \times 1.2 \times 1.0$  normalized), and an unusual radar shape, which in this case looks something like a kidney bean (Mitchell *et al.* 1998). The origin of Eros’s distinct convex side may be related to that of the analogous feature found on Geographos. Since the NEAR spacecraft is targeted to arrive at Eros in 1999, *in situ* studies will shortly be able to substantiate or refute this hypothesis.

Three of the ECAs imaged so far by delay-Doppler radar techniques (4769 Castalia, 2063 Bacchus, and 4179 Toutatis) have double-lobed shapes. Our results suggest they may have been influenced or even created by planetary tidal forces.

4769 Castalia has dimensions of  $0.7 \times 1.0 \times 1.6$  km, giving it an ellipticity of  $\varepsilon = 0.47$  (Hudson and Ostro 1994). Its fast rotation rate ( $P = 4$  h) and favorable orbital parameters ( $a = 1.06$  AU,  $e = 0.48$ ,  $i = 8.9^\circ$ , allowing it to cross the orbits of both Earth and Venus with  $v_\infty \sim 16$  km  $\text{s}^{-1}$ ), make it a good candidate for tidal disruption.

2063 Bacchus, an ECA on a Castalia-like orbit ( $a = 1.08$  AU,  $e = 0.35$ ,  $i = 9.4^\circ$ ), can encounter Earth and Venus at even lower  $v_\infty$  ( $\sim 10$ – $11$  km  $\text{s}^{-1}$ ). Its rotation period, however, is much longer (nearly 15 h; Benner *et al.* 1997).

4179 Toutatis ( $a = 2.52$  AU,  $e = 0.635$ ,  $i = 0.472^\circ$ ) is an ECA with dimensions of  $1.92 \times 2.40 \times 4.60$  km ( $\varepsilon = 0.53$ ). It is in a tumbling rotation state with a period of 130 h (Hudson and Ostro 1995, G. Black 1997, pers. commun.). Its very low inclination, however, makes it five times more likely to encounter Earth at  $v_\infty \sim 12$  km  $\text{s}^{-1}$  than a typical ECA.

Our results indicate that double-lobed objects may be produced by weak S-class or strong B-class events, where large similar-sized components typically near the center of the fragment train often bump into one another at such gentle speeds and with sufficient rotation that the new aggregate retains a double-lobed shape. For example, the  $P = 6$  h,  $q = 1.8 R_\oplus$ ,  $v_\infty = 6$  km  $\text{s}^{-1}$  outcome shown in Fig. 5 produces such a contact binary (see Fig. 12a for a close-up view; also see Table I). The run with  $P = 10$  h,  $q = 1.6 R_\oplus$ , and  $v_\infty = 8$  km  $\text{s}^{-1}$  does as well (Fig. 12b). Both objects have properties roughly consistent with Jacobi ellipsoids (Binney and Tremaine 1987, their Fig. 4-17), which indicates that the objects are in rotational fluid equilibrium: the former has a spin of 5.0 h, axis ratios  $q_2 = 0.48$ ,  $q_3 = 0.42$ , and bulk density  $1.8$  g  $\text{cm}^{-3}$ ; the latter has a spin of 5.3 h, axis ratios  $q_2 = 0.36$ ,  $q_3 = 0.34$ , and bulk density  $2.0$  g  $\text{cm}^{-3}$ .

*4.1.6. Size and orbital distribution of ECAs: Evidence for tidal disruption?* Tidal disruption, occurring at low  $v_\infty$ , may produce enough small bodies to enhance the local population. A qualitative check by Bottke *et al.* (1998a) of the size and orbital distribution of the known ECA population shows few large bodies but many small bodies with low  $e$  and  $i$ . These features may be consistent with tidal disruption, though we cannot say how much the known ECA population suffers from observational selection effects (Jedicke 1996, Jedicke and Metcalfe 1998). These results may also explain the population of small Earth-crossing objects inferred from Spacewatch data (Rabinowitz *et al.* 1993, Rabinowitz 1994), a possibility also suggested by Asphaug and Benz (1996a) and Solem and Hills (1996).

## 4.2. Future Work

In this paper, we have explored many of the parameters important for tidal disruption: trajectory ( $q$ ,  $v_\infty$ ), rotation ( $P$ ), spin axis orientation ( $\alpha$ ,  $\beta$ ), shape, long-axis rotational phase angle ( $\theta$ ), and density. Practical considerations prevented systematic exploration over all possible ranges of these variables that lead to tidal disruption, but we feel that we have obtained a good understanding of the basic encounter outcomes. Higher resolution sampling in the

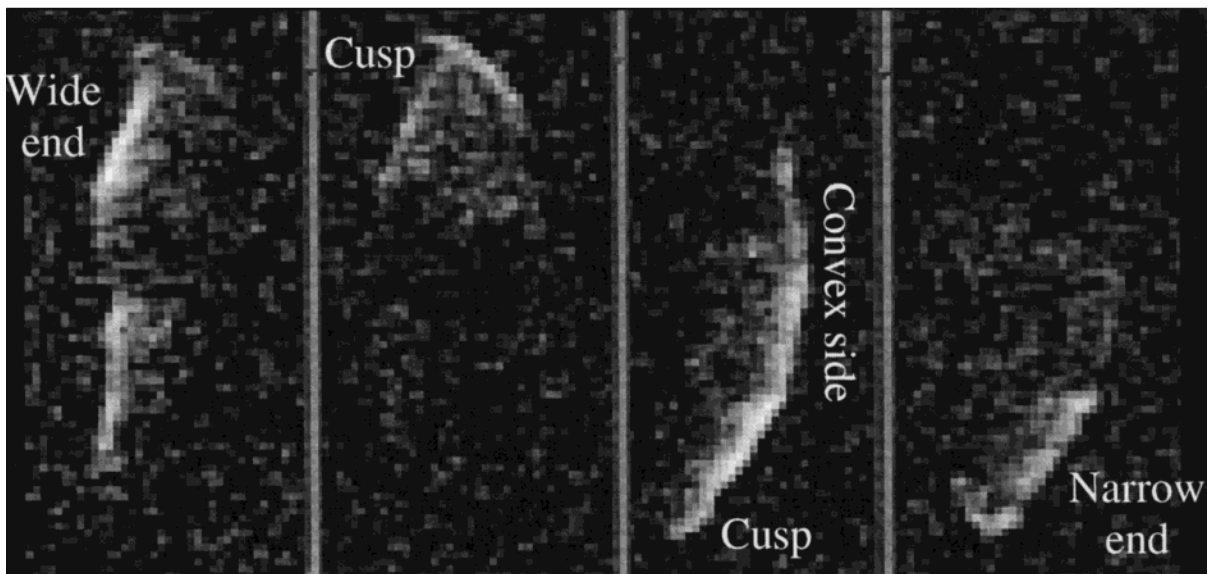
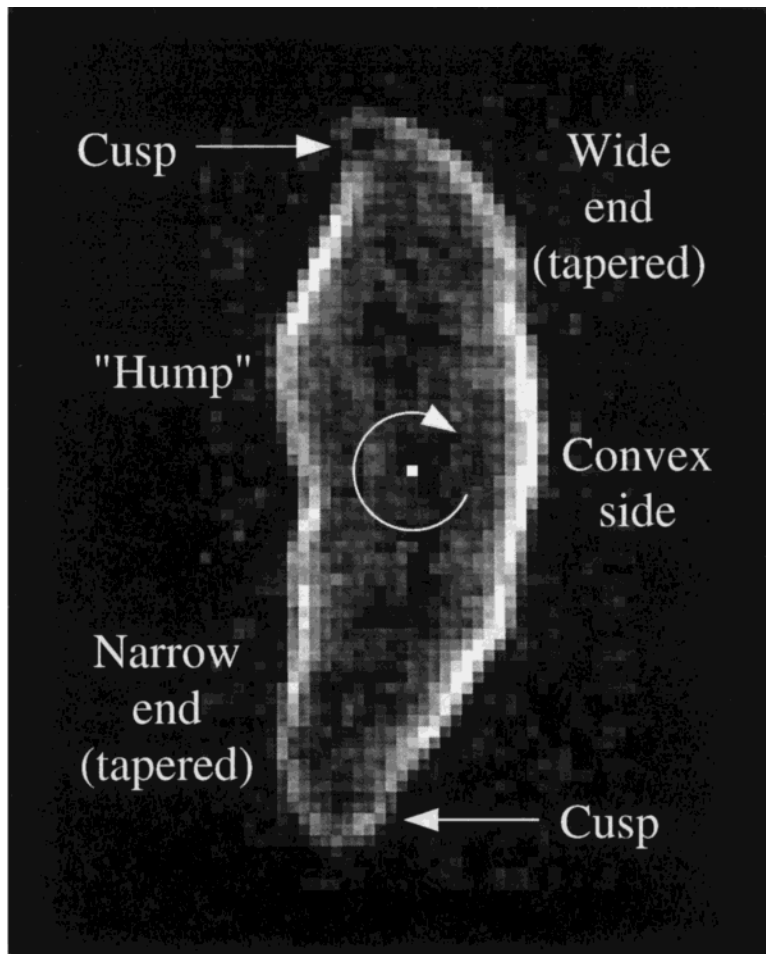


**FIG. 11.** Pole-on silhouette of 1620 Geographos determined from delay-Doppler radar techniques (Ostro *et al.* 1995a, Ostro *et al.* 1996). This image has been constructed from multi-run sums of 12 co-registered images, each  $30^\circ$  wide in phase space. The central white pixel indicates the body's center-of-mass; rotation direction is indicated by the circular arrow. Brightness indicates the strength of radar return, arbitrarily scaled. Despite substantial smearing of the peripheral features, some distinguishing characteristics can be seen: (1) the long axis is tapered at both ends, with one end narrower than the other; (2) one side is smooth and convex; (3) cusps at each end are swept back against the rotation direction, giving the body the appearance of a pinwheel. The frames at the bottom show 4 of the 12 images used to make this silhouette. The resolution is  $500 \text{ ns} \times 1.64 \text{ Hz}$  ( $75 \times 87 \text{ m}$ ).

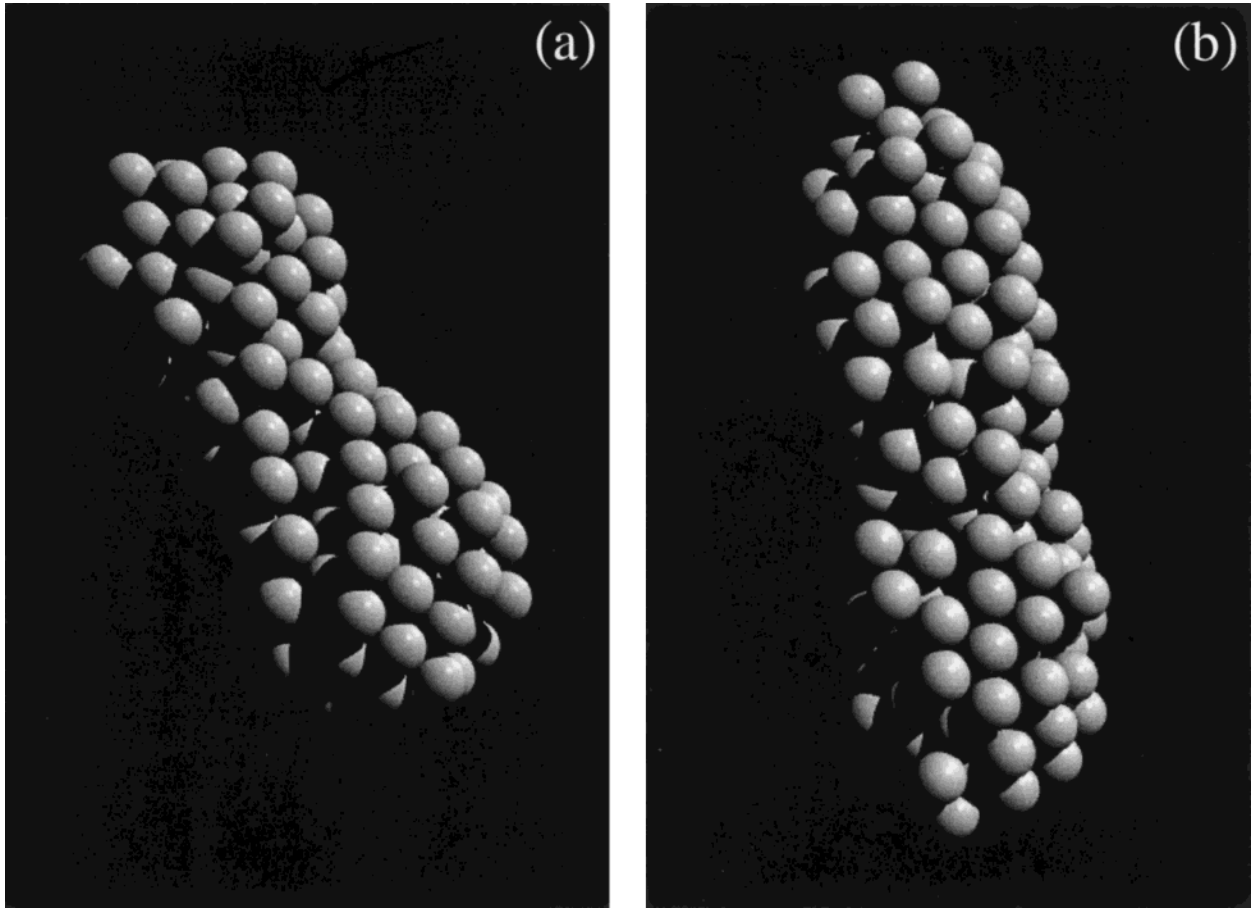


**FIG. 12.** Two examples of contact binaries formed by coalescence of nearly equal-sized fragments following B-class disruption of an elongated rubble-pile asteroid. The encounter parameters were: (a)  $P = 6$  h,  $q = 1.8 R_{\oplus}$ ,  $v_{\infty} = 6$  km s $^{-1}$ , and (b)  $P = 10$  h,  $q = 1.6 R_{\oplus}$ ,  $v_{\infty} = 8$  km s $^{-1}$ . Remnant (a) has a spin of 5.0 h and dimensions  $3.1 \times 1.5 \times 1.3$  km; remnant (b) has a spin of 5.3 h and dimensions  $3.8 \times 1.4 \times 1.3$  km. Both objects are close to rotational fluid equilibrium.

$q$ - $v_{\infty}$ - $P$  space is desirable, but unlikely to yield much in the way of new results. A more thorough investigation of progenitor shape effects is probably of greater importance, along with a better understanding of the role of  $\alpha$ ,  $\beta$ , and  $\theta$ . As computer power and availability improve, we plan to explore these issues in greater detail.

We also intend to explore the internal structure of the rubble pile itself. Although more sophisticated than previous studies, our model is nonetheless crude. One refinement would be to increase the resolution by including more particles, but this would require considerably more computation time. A few representative cases may allow us to estimate the importance of higher resolution (we have done this to a certain extent already, and found that higher resolution smooths out the boundary between M- and N-class disruption). A second refinement would be to examine rubble piles that have a nonuniform particle size distribution. Clump formation may be enhanced by the use of a size distribution since the larger particles become

natural seeds for agglomeration of the smaller ones (Richardson *et al.* 1995). Smaller particles could also fill the gaps between larger particles, leading to higher bulk densities. It would also be interesting to consider the effects of more realistic nonspherical constituent particles. Interlocking between such particles could lead to even larger potential energy barriers allowing the formation of irregular shaped rubble piles. However, nonspherical aggregates are much harder to implement numerically than simple spheres. More readily testable is the inclusion of surface friction between the spheres, although preliminary investigation of this effect shows that it manifests itself only as a slightly increased damping without changing the outcome very much (Richardson *et al.* 1995).

Finally, with the data already in hand, it may be possible to develop an analytical theory to predict tidal disruption outcomes on the basis of the parameters explored here. Some steps toward this end have been taken already (cf. Section 3.1), but much remains to be done.

It is our belief that tidal disruption and studies of rubble piles in general will continue to be a fruitful line of research in the field of planetary science. Ultimately such research may contribute to a unified model of small bodies in the Solar System that combines both orbital and physical evolution.

## APPENDIX A. ENCOUNTER TIME

For a point particle on a hyperbolic trajectory, the time since close approach is given by Goldstein (1980),

$$t = \sqrt{\frac{a^3}{GM_\oplus}} \int_0^F (e \cosh F - 1) dF, \quad (13)$$

where  $a$  is the semimajor axis of the orbit,  $e$  is the orbital eccentricity ( $e > 1$ ), and  $F$  is the hyperbolic analog of the eccentric anomaly defined by

$$r = a(e \cosh F - 1), \quad (14)$$

where  $r$  is the distance from the central mass, in our case Earth. The orbital elements can be obtained from (Goldstein 1980),

$$\frac{1}{a} = \frac{v^2}{GM_\oplus} - \frac{2}{r}, \quad (15)$$

where  $v$  is the orbital speed with respect to Earth, and

$$q = a(e - 1). \quad (16)$$

Equation (15) can be written in terms of  $v_\infty$  by setting  $r \rightarrow \infty$ :

$$\frac{1}{a} = \frac{v_\infty^2}{GM_\oplus}. \quad (17)$$

Hence if the initial distance ( $15 R_{\text{Roche}}$ ) is  $r_i$  and the final distance ( $60 R_\oplus$ ) is  $r_f$ , then the total encounter time is given by

$$T = \sqrt{\frac{a^3}{GM_\oplus}} [e(\sinh F_i + \sinh F_f) - (F_i + F_f)], \quad (18)$$

where

$$F_i = \cosh^{-1} \left[ \frac{1}{e} \left( 1 + \frac{r_i}{a} \right) \right] \quad (19)$$

and

$$F_f = \cosh^{-1} \left[ \frac{1}{e} \left( 1 + \frac{r_f}{a} \right) \right]. \quad (20)$$

For example, the S-class run shown in Fig. 2 had a total encounter time of 30.1 h, of which 1.3 h was spent within the Roche limit ( $3.4 R_\oplus$ ). By contrast, the  $q = 3 R_\oplus$ ,  $v_\infty = 9 \text{ km s}^{-1}$  N-class run in Table I had an encounter time of 21.1 h and spent only 34 min at the edge of the tidal limit.

Note that a rubble pile is not a point particle and therefore experiences changes in orbital energy and angular momentum as a result of a tidal encounter, with corresponding changes in  $a$  and  $e$ . However, in all the cases considered here, the difference in the encounter time due to this effect is negligible. This would not be the case for very nearly parabolic orbits however, where some particles near the inner edge of the rubble

pile could actually be captured into orbit by the planet (Stevenson *et al.* 1986; Bottke *et al.* in preparation).

## APPENDIX B. CRATER CHAINS ON EARTH AND THE MOON: SEMI-ANALYTICAL DERIVATION

The number of ECAs larger than a given diameter  $D$  that pass a distance  $r$  from the center of Earth without striking Earth is given by

$$F_{\text{Earth}} = P_i N_D \left\{ r^2 \left[ 1 + \frac{v_{\text{esc},\oplus}^2(r)}{v_\infty^2} \right] - R_\oplus^2 \left[ 1 + \frac{v_{\text{esc},\oplus}^2(R_\oplus)}{v_\infty^2} \right] \right\}, \quad (21)$$

where

$$v_{\text{esc},\oplus}(r) = \sqrt{\frac{2GM_\oplus}{r}} \quad (22)$$

is the escape speed from Earth at a distance  $r$  from its center,  $R_\oplus$  and  $M_\oplus$  are the radius and mass of Earth, respectively,  $v_\infty$  is the speed of the asteroid before the gravitational acceleration of Earth is included,  $P_i$  is the intrinsic collision probability of ECAs with Earth (Bottke *et al.* 1994a,b), and  $N_D$  is the cumulative number of ECAs larger than  $D$ . The number of bodies that pass through this annulus to strike the Moon is

$$F_{\text{Moon Impact}} = F_{\text{Earth}} \left( \frac{\pi R_\text{Moon}^2}{4\pi d^2} \right) \left[ 1 + \frac{v_{\text{esc},\text{Moon}}^2(R_\text{Moon})}{v_\infty^2 + v_{\text{esc},\oplus}^2(d)} \right], \quad (23)$$

where

$$v_{\text{esc},\text{Moon}}(r) = \sqrt{\frac{2GM_\text{Moon}}{r}} \quad (24)$$

is the escape speed from the Moon at a distance  $r$  from its center,  $R_\text{Moon}$  and  $M_\text{Moon}$  are the radius and mass of the Moon, respectively, and  $d$  is the Moon's distance from Earth.

To estimate the flux of crater chains formed on the Moon over time, we define the parameter  $r_{\text{S},\oplus}$ , the minimum Earth approach distance needed for an asteroid to undergo an S-class event,

$$r_{\text{S},\oplus} = f_{\text{S},\oplus} R_\oplus, \quad (25)$$

where  $f_{\text{S},\oplus}$  is a dimensionless factor that depends on quantities such as the progenitor's encounter speed, its spin period, its bulk density, etc. Note that  $r_{\text{S},\oplus}$  currently can only be found numerically, but that the final result is comparable to Eq. (3). The escape speed at  $r_{\text{S},\oplus}$  is then given by

$$v_{\text{esc},\oplus}(r_{\text{S},\oplus}) = \sqrt{\frac{2GM_\oplus}{r_{\text{S},\oplus}}} = f_{\text{S},\oplus}^{1/2} v_{\text{esc},\oplus}(R_\oplus), \quad (26)$$

allowing us to rewrite Eq. (21) as:

$$F_{\text{Earth}} = P_i N_D R_\oplus^2 \left[ (f_{\text{S},\oplus}^2 - 1) + (f_{\text{S},\oplus} - 1) \frac{v_{\text{esc},\oplus}^2(R_\oplus)}{v_\infty^2} \right]. \quad (27)$$

We now perform the analogous steps for objects disrupted by the Moon. The number of ECAs larger than a given diameter  $D$  that pass within a distance  $r$  from the Moon without striking it is given by

$$F_{\text{Moon}} = P_i N_D \left\{ r_\text{Moon}^2 \left[ 1 + \frac{v_{\text{esc},\text{Moon}}^2(r)}{v_\infty^2 + v_{\text{esc},\oplus}^2(d)} \right] - R_\text{Moon}^2 \left[ 1 + \frac{v_{\text{esc},\text{Moon}}^2(R_\text{Moon})}{v_\infty^2 + v_{\text{esc},\oplus}^2(d)} \right] \right\}, \quad (28)$$

where we have accounted for the acceleration of the objects due to Earth.

The number of bodies undergoing S-class events (a distance  $r_{s,\text{D}}$  from the Moon) is therefore

$$F_{\text{Moon}} = P_i N_D R_\oplus^2 \left[ (f_{s,\text{D}}^2 - 1) + (f_{s,\text{D}} - 1) \frac{v_{\text{esc},\text{D}}^2(R_\oplus)}{v_\infty^2 + v_{\text{esc},\text{D}}^2(d)} \right], \quad (29)$$

where  $f_{s,\text{D}}$  is the equivalent of  $f_{s,\oplus}$  for the Moon. Finally, the number of bodies that disrupt near the Moon and go on to hit Earth is given by

$$F_{\text{Earth Impact}} = F_{\text{Moon}} \left( \frac{\pi R_\oplus^2}{4\pi d^2} \right) \left[ 1 + \frac{v_{\text{esc},\oplus}^2(R_\oplus)}{v_\infty^2} \right]. \quad (30)$$

Taking the ratio of the flux of crater chains formed on the Moon ( $F_{\text{Moon Impact}}$ ) to that of Earth ( $F_{\text{Earth Impact}}$ ), we find that many parameters drop out of the equation, leaving

$$\frac{F_{\text{Moon Impact}}}{F_{\text{Earth Impact}}} = \frac{\left[ (f_{s,\oplus}^2 - 1) + (f_{s,\oplus} - 1) \left( \frac{v_{\text{esc},\oplus}^2(R_\oplus)}{v_\infty^2} \right) \right] \left[ 1 + \frac{v_{\text{esc},\text{D}}^2(R_\oplus)}{v_\infty^2 + v_{\text{esc},\oplus}^2(d)} \right]}{\left[ (f_{s,\text{D}}^2 - 1) + (f_{s,\text{D}} - 1) \left( \frac{v_{\text{esc},\text{D}}^2(R_\oplus)}{v_\infty^2 + v_{\text{esc},\oplus}^2(d)} \right) \right] \left[ 1 + \frac{v_{\text{esc},\oplus}^2(R_\oplus)}{v_\infty^2} \right]}. \quad (31)$$

The remaining variables,  $f_{s,\text{D}}$ ,  $f_{s,\oplus}$ , and  $v_\infty$  can be estimated from Fig. 4 and Fig. 9. For rubble piles with rotation periods of 6 h,  $f_{s,\text{D}} \sim 1.1$  for  $v_\infty = 3 \text{ km s}^{-1}$ , while  $f_{s,\oplus} = 2.2, 1.4, 1.4$  for  $v_\infty = 3, 6, 9 \text{ km s}^{-1}$ , respectively. Negligible mass shedding occurs at higher velocities. Substituting and taking the ratio, we find that about nine crater chains are made on the Moon for every one that is made on Earth. Using more exact measurements, Bottke *et al.* (1997) found this ratio was  $\sim 10$ , a very good match. Since only one or two crater chains have been formed on the Moon over the past 3.8 Gyr, it seems unlikely that any crater chains have been formed on Earth within the past few hundred million years.

## ACKNOWLEDGMENTS

This research was supported by D.C.R.'s Natural Sciences and Engineering Research Council (NSERC) Fellowship at the Canadian Institute for Theoretical Astrophysics (CITA) and grants from the NASA Innovative Research Program and NASA HPCC/ESS; W.F.B.'s Texaco Prize Fellowship at Caltech; and S.G.L.'s O. K. Earl Prize Fellowship at Caltech. Preparation of the paper was partly supported by NASA Grant NAGW-310 to J. A. Burns. The authors thank Erik Asphaug, Lance Benner, Joe Burns, Anthony Dobrovolskis, Paolo Farinella, Alan Harris, Jay Melosh, Patrick Michel, Steven Ostro, Paul Weissman, and an anonymous reviewer for their valued contributions to this project. The ray-traced images featured in this paper were constructed using the Persistence of Vision Ray Tracer (POV-Ray 3.01).

## REFERENCES

- Aarseth, S. J. 1985. Direct methods for  $N$ -body simulations. In *Multiple Time Scales* (J. U. Brackbill and B. I. Cohen, Eds.), pp. 377–418. Academic Press, New York.
- Aggarwal, H. R., and V. R. Oberbeck 1974. Roche limit of a solid body. *Astrophys. J.* **191**, 577–588.
- Asphaug, E., and W. Benz 1994. Density of Comet Shoemaker-Levy 9 deduced by modelling breakup of the parent “rubble pile.” *Nature* **370**, 120–124.
- Asphaug, E., and W. Benz 1996. Size, density, and structure of Comet Shoemaker-Levy-9 inferred from the physics of tidal breakup. *Icarus* **121**, 225–248.
- Asphaug, E., and H. J. Melosh 1993. The Stickney impact of Phobos—A dynamic model. *Icarus* **101**, 144–164.
- Asphaug, E., W. Benz, S. J. Ostro, D. J. Scheeres, E. M. De Jong, S. Suzuki, and R. S. Hudson 1996. Disruptive impacts into small asteroids. *Bull. Am. Astron. Soc.* **28**, 1102.
- Belton, M. J. S., and 19 colleagues 1994a. Galileo encounter with 951 Gaspra: First pictures of an asteroid. *Science* **257**, 1647–1652.
- Belton, M. J. S., and 19 colleagues 1994b. First images of asteroid 243 Ida. *Science* **265**, 1543–1547.
- Belton, M. J. S., and 16 colleagues 1995. Bulk density of asteroid 243-Ida from the orbit of its satellite Dactyl. *Nature* **374**, 785–788.
- Benner, L. A. M., and 15 colleagues 1997. Radar observations of Near-Earth Asteroid 2063 Bacchus. *Bull. Am. Astron. Soc.* **29**, 965.
- Benz, W., and E. Asphaug 1994. Impact simulations with fracture. I. Method and tests. *Icarus* **107**, 98–116.
- Benz, W., and J. G. Hills 1987. Three-dimensional hydrodynamical simulations of stellar collisions. I. Equal-mass main-sequence stars. *Astrophys. J.* **323**, 614–628.
- Benz, W., J. G. Hills, and F.-K. Thielemann 1989. Three-dimensional hydrodynamical simulations of stellar collisions. II. White dwarfs. *Astrophys. J.* **342**, 986–998.
- Binney, J., and S. Tremaine 1987. *Galactic Dynamics*. Princeton Univ. Press, Princeton, NJ.
- Boss, A. P. 1994. Tidal disruption of periodic Comet Shoemaker-Levy-9 and a constraint on its mean density. *Icarus* **107**, 422–426.
- Boss, A. P., A. G. W. Cameron, and W. Benz 1991. Tidal disruption of inviscid planetesimals. *Icarus* **92**, 165–178.
- Bottke, W. F., and H. J. Melosh 1996a. The formation of asteroid satellites and doublet craters by planetary tidal forces. *Nature* **381**, 51–53.
- Bottke, W. F., and H. J. Melosh 1996b. The formation of binary asteroids and doublet craters. *Icarus* **124**, 372–391.
- Bottke, W. F., M. C. Nolan, and R. Greenberg 1994a. Velocity distributions among colliding asteroids. *Icarus* **107**, 255–268.
- Bottke, W. F., M. C. Nolan, R. Greenberg, and R. A. Kolvoord 1994b. Collisional lifetimes and impact statistics of near-Earth asteroids. In *Hazards Due to Comets and Asteroids* (T. Gehrels and M. S. Matthews, Eds.), pp. 337–357. Univ. of Arizona Press, Tucson.
- Bottke, W. F., D. C. Richardson, and S. G. Love 1997. Can tidal disruption of asteroids make crater chains on the Earth and Moon? *Icarus* **126**, 470–474.
- Bottke, W. F., D. C. Richardson, and S. G. Love 1998a. Production of Tunguska-sized bodies by Earth's tidal forces. *Planet Space Sci.* **46**, 311–322.
- Bottke, W. F., D. C. Richardson, P. Michel, and S. G. Love 1998b. 1620 Geographos and 433 Eros: Resculpted by planetary tides. Submitted for publication.
- Burns, J. A., and V. S. Safronov 1973. Asteroid nutation angles. *Mon. Not. R. Astron. Soc.* **165**, 403–411.
- Chapman, C. R. 1978. Asteroid collisions, craters, regolith, and lifetimes. In *Asteroids: An Exploration Assessment* (D. Morrison and W. C. Wells, Eds.), NASA Conf. Publ. 2053, pp. 145–160.
- Chandrasekhar, S. 1969. *Ellipsoidal Figures of Equilibrium*. Yale Univ. Press, New Haven, CT.
- Chauvineau, B., P. Farinella, and A. W. Harris 1995. The evolution of Earth-approaching binary asteroids: A Monte-Carlo dynamical model. *Icarus* **115**, 36–46.
- Cook, C. M., H. J. Melosh, and W. F. Bottke 1998. Doublet craters on Venus. *J. Geophys. Res. Planets*, in press.
- Dobrovolskis, A. R. 1982. Internal stresses in Phobos and other triaxial bodies. *Icarus* **52**, 136–148.

- Dobrovolskis, A. R. 1990. Tidal disruption of solid bodies. *Icarus* **88**, 24–38.
- Farinella, P. 1992. Evolution of Earth-crossing binary asteroids due to gravitational encounters with the Earth. *Icarus* **96**, 284–285.
- Farinella, P., and B. Chauvineau 1993. On the evolution of binary Earth-approaching asteroids. *Astron. Astrophys.* **279**, 251–259.
- Gladman, B. J., F. Migliorini, A. Morbidelli, V. Zappalà, P. Michel, A. Cellino, C. Froeschlé, H. F. Levison, M. Bailey, and M. Duncan 1997. Dynamical lifetimes of objects injected into asteroid belt resonances. *Science* **277**, 197–201.
- Goldstein, H. 1980. *Classical Mechanics*, 2nd ed. Addison-Wesley, Reading.
- Greenberg, R., M. C. Nolan, W. F. Bottke, R. A. Kolvoord, and J. Veverka 1994. Collisional history of Gaspra. *Icarus* **107**, 84–97.
- Greenberg, R., W. F. Bottke, M. C. Nolan, P. Geissler, J.-M. Petit, D. D. Durda, E. Asphaug, and J. Head 1996. Collisional and dynamical history of Ida. *Icarus* **120**, 106–118.
- Hahn, J. M., and T. W. Rettig 1998. Tidal disruption of strengthless rubble piles—A timescale analysis. *Planet Space Sci.*, in press.
- Harris, A. W. 1994. Tumbling asteroids. *Icarus* **107**, 209–211.
- Harris, A. W. 1996. The rotation rates of very small asteroids: Evidence for “rubble-pile” structure. *Lunar Planet. Sci. 27th*, 493–494.
- Hudson, R. S., and S. J. Ostro 1994. Shape of asteroid 4769 Castalia (1989 PB) from inversion of radar images. *Science* **263**, 940–943.
- Hudson, R. S., and S. J. Ostro 1995. Shape and non-principal axis spin-state of asteroid 4179 Toutatis. *Science* **270**, 84–86.
- Jedicke, R. 1996. Detection of near Earth asteroids based upon their rates of motion. *Astron. J.* **111**, 970–982.
- Jedicke, R., and T. S. Metcalfe 1998. The orbital and absolute magnitude distributions of main belt asteroids. *Icarus* **131**, 245–260.
- Jeffreys, H. 1947. The relation of cohesion to Roche’s limit. *Mon. Not. R. Astron. Soc.* **107**, 260–272.
- Kaula, W. M., and A. E. Beachey 1984. Mechanical models of close approaches and collisions of large protoplanets. In *Origin of the Moon* (W. K. Hartmann, R. J. Phillips, and G. J. Taylor, Eds.), pp. 567–576. Lunar and Planetary Institute, Houston.
- Love, S. G., and T. J. Ahrens 1996. Catastrophic impacts on gravity dominated asteroids. *Icarus* **124**, 141–155.
- Love, S. G., D. E. Brownlee, N. L. King, and F. Hörz 1995. Morphology of meteoroid and debris impact craters formed in soft metal targets on the LDEF satellite. *Int. J. Impact Eng.* **16**, 405–418.
- Love, S. G., F. Hörz, and D. E. Brownlee 1993. Target porosity effects in impact cratering and collisional disruption. *Icarus* **105**, 216–224.
- McFadden, L. A., D. J. Tholen, and G. J. Veeder 1989. Physical properties of Aten, Apollo, and Amor asteroids. In *Asteroids II* (R. P. Binzel, T. Gehrels, and M. S. Matthews, Eds.), pp. 442–467. Univ. of Arizona Press, Tucson.
- Melosh, H. J. 1989. *Impact Cratering: A Geologic Process*. Oxford Univ. Press, New York.
- Melosh, H. J., and E. V. Ryan 1997. Asteroids: Shattered but not dispersed. *Icarus* **129**, 562–564.
- Melosh, H. J., and P. Schenk 1993. Split comets and the origin of crater chains on Ganymede and Callisto. *Nature* **365**, 731–733.
- Melosh, H. J., and J. A. Stansberry 1991. Doublet craters and the tidal disruption of binary asteroids. *Icarus* **94**, 171–179.
- Melosh, H. J., and E. A. Whitaker 1994. Lunar crater chains. *Nature* **369**, 713–714.
- Melosh, H. J., J. Ingram, and W. F. Bottke 1996. The abundance of doublet craters on Mars. *Lunar Planet. Sci.* **27**, 863.
- Menichella, M., P. Paolicchi, and P. Farinella 1996. The main-belt as a source of near-Earth asteroids. *Earth Moon Planets* **72**, 133–149.
- Michel, P., Ch. Froeschlé, and P. Farinella 1996. Dynamical evolution of NEAs—Close encounters, secular perturbations and resonances. *Earth Moon Planets* **72**, 151–164.
- Milani, A., M. Carpino, G. Hahn, and A. M. Nobili 1989. Dynamics of planet-crossing asteroids—Classes of orbital behavior. *Icarus* **78**, 212–269.
- Mitchell, D. L., R. S. Hudson, S. J. Ostro, and K. D. Rosema 1998. Shape of asteroid 433 Eros from inversion of Goldstone radar Doppler spectra. *Icarus* **131**, 4–14.
- Mizuno, H., and A. P. Boss 1985. Tidal disruption of dissipative planetesimals. *Astron. J.* **63**, 109–133.
- Morbidelli, A., and M. Moons 1995. Numerical evidence on the chaotic nature of the 3/1 mean motion commensurability. *Icarus* **115**, 60–65.
- Morrison, D., Ed. 1992. *The Spaceguard Survey*, Report of the NASA near-Earth object detection workshop. NASA, Washington, DC.
- Mottola, S., G. Hahn, P. Pravec, and L. Sarounova 1997. S/1997 (3671) 1. IAU Circular 6680.
- Ocampo, S. C., and K. O. Pope 1996. Shuttle imaging radar SIR-C: Images reveal multiple craters at Aorounga, northern Chad. *Lunar Planet. Sci.* **27**, 977–978.
- Öpik, E. J. 1950. Roche’s limit: Rings of Saturn. *Irish Astron. J.* **1**, 25–26.
- Öpik, E. J. 1966. Sun-grazing comets and tidal disruption. *Irish Astron. J.* **7**, 141–161.
- Ostro, S. J. 1993. Planetary radar astronomy. *Rev. Mod. Phys.* **65**, 1235–1279.
- Ostro, S. J., and 11 colleagues 1995a. Extreme elongation of asteroid 1620 Geographos from radar images. *Nature* **375**, 474–477.
- Ostro, S. J., and 13 colleagues 1995b. Radar images of asteroid 4179 Toutatis. *Science* **270**, 80–83.
- Ostro, S. J., and 12 colleagues 1996. Radar observations of asteroid 1620 Geographos. *Icarus* **121**, 46–66.
- Petit, J.-M., and M. Hénon 1987. A numerical simulation of planetary rings. I. Binary encounters. *Astron. Astrophys.* **173**, 389–404.
- Pöschel, T., and V. Buchholtz 1993. Static friction phenomena in granular materials: Coulomb law versus particle geometry. *Phys. Rev. Lett.* **71**, 3963–3966.
- Pravec, P., and G. Hahn 1997. Two-period lightcurve of 1994 AW<sub>1</sub>: Indication of a binary asteroid? *Icarus* **127**, 431–440.
- Press, W. H., and D. N. Spergel 1988. Choice of order and extrapolation method in Aarseth-type *N*-body algorithms. *Astrophys. J.* **325**, 715–721.
- Press, W. H., S. A. Teukolsky, W. T. Vetterling, and B. P. Flannery 1992. *Numerical Recipes in C: The Art of Scientific Computing*, 2nd ed. Cambridge Univ. Press, Cambridge.
- Rabinowitz, D. L. 1994. The size and shape of the near-Earth asteroid belt. *Icarus* **111**, 364–377.
- Rabinowitz, D. L., T. Gehrels, J. V. Scotti, R. S. McMillan, M. L. Perry, W. Wisniewski, S. M. Larson, E. S. Howell, and B. E. A. Mueller 1993. Evidence for a near-Earth asteroid belt. *Nature* **363**, 704–706.
- Rampino, M. R., and T. Volk 1996. Multiple impact event in the Paleozoic: Collision with a string of comets or asteroids? *Geophys. Res. Lett.* **23**, 49–52.
- Rettig, T. W., M. J. Mumma, G. J. Sobczak, J. M. Hahn, and M. DiSanti 1996. The nature of Comet Shoemaker-Levy 9 subnuclei from analysis of preimpact Hubble Space Telescope images. *J. Geophys. Res.* **101**, 9271–9281.
- Richardson, D. C. 1993. A new tree code method for simulations of planetesimal dynamics. *Mon. Not. R. Astron. Soc.* **261**, 396–414.

- Richardson, D. C. 1994. Tree code simulations of planetary rings. *Mon. Not. R. Astron. Soc.* **269**, 493–511.
- Richardson, D. C. 1995. A self-consistent numerical treatment of fractal aggregate dynamics. *Icarus* **115**, 320–335.
- Richardson, D. C., E. Asphaug, and L. Benner 1995. Comet Shoemaker–Levy 9: A “rubble pile” model with dissipative collisions and gravitational perturbations. *Bull. Am. Astron. Soc.* **27**, 1114.
- Rickman, H. 1979. Recent dynamical history of the six short-period comets discovered in 1975. In *Dynamics of the Solar System* (R. L. Duncombe, Ed.), pp. 293–298. D. Reidel, Dordrecht.
- Rickman, H., and A. M. Malmort 1981. Variations of the orbit of comet P/Gehrels 3: Temporary satellite captures by Jupiter. *Astron Astrophys.* **102**, 165–170.
- Schenk, P. M., E. Asphaug, W. B. McKinnon, H. J. Melosh, and P. R. Weissman 1996. Cometary nuclei and tidal disruption: The geologic record of crater chains on Callisto and Ganymede. *Icarus* **121**, 249–274.
- Schultz, P. H., and D. E. Gault 1985. Clustered impacts: Experiments and implications. *J. Geophys. Res.* **90**, 3701–3732.
- Sekiguchi, N. 1970. On the fission of a solid body under influence of tidal force. *Moon* **1**, 429–439.
- Sekanina, Z., and D. K. Yeomans 1985. Orbital motion, nucleus precession, and splitting of periodic Comet Brooks 2. *Astron. J.* **90**, 2335–2352.
- Sekanina, Z., P. W. Chodas, and D. K. Yeomans 1994. Tidal disruption and the appearance of periodic Comet Shoemaker–Levy 9. *Astron. Astrophys.* **289**, 607–636.
- Solem, J. C., and J. G. Hills 1996. Shaping of Earth-crossing asteroids by tidal forces. *Astron. J.* **111**, 1382–1387.
- Sridhar, S., and S. Tremaine 1992. Tidal disruption of viscous bodies. *Icarus* **95**, 86–99.
- Stevenson, D. J., A. W. Harris, and J. I. Lunine 1986. Origins of satellites. In *Satellites* (J. A. Burns and M. S. Matthews, Eds.), pp. 39–88. Univ. of Arizona Press, Tucson.
- Thomas, P., M. J. S. Belton, B. Carcich, C. R. Chapman, M. E. Davies, R. Sullivan, and J. Veverka 1996. The shape of Ida. *Icarus* **120**, 20–32.
- Thomas, P., J. Veverka, J. Bell, J. Lunine, and D. Cruikshank 1992. Satellites of Mars: Geologic history. In *Mars* (H. H. Kieffer, B. M. Jakosky, C. W. Snyder, and M. S. Matthews, Eds.), pp. 1257–1282. Univ. of Arizona Press, Tucson.
- Wasson, J. T. 1985. *Meteorites—Their Record of Early Solar System History*. Freeman, New York.
- Watanabe, S., and S. M. Miyama 1992. Collision and tidal interaction between planetesimals. *Astrophys. J.* **391**, 318–335.
- Weidenschilling, S. J. 1997. The origin of comets in the solar nebula: A unified model. *Icarus* **127**, 290–306.
- Weissman, P. R. 1980. Physical loss of long-period comets. *Astron. Astrophys.* **85**, 191–196.
- Weissman, P. R. 1982. Terrestrial impact rates for long- and short-period comets. *GSA Special Paper* **190**, 15–24.
- Wisdom, J. 1983. Chaotic behavior and the origin of the 3/1 resonance. *Icarus* **56**, 51–74.
- Wichman, R. W., and C. A. Wood 1995. The Davy crater chain: Implications for tidal disruption in the Earth–Moon system and elsewhere. *Geophys. Res. Lett.* **22**, 583–586.
- Yeomans, D. K., and 12 colleagues 1997. Estimating the mass of asteroid 253 Mathilde from tracking data during the NEAR flyby. *Science* **278**, 2106–2109.
- Yoder, C. F. 1982. Tidal rigidity of Phobos. *Icarus* **49**, 327–346.